Title:
"Robust estimates of the ratio between S- and P-wave velocity anomalies in the Earth's mantle using normal modes"

Federica Restelli[1], Christophe Zaroli[2] & Paula Koelemeijer[3]

[1] Royal Holloway University of London, federica.restelli.2019@live.rhul.ac.uk
[2] Université de Strasbourg, c.zaroli@unistra.fr
[3] University of Oxford, paula.koelemeijer@earth.ox.ac.uk

The paper is a non-peer reviewed pre-print submitted to EarthArXiv. The paper has been submitted to the SEDI special issue of *Physics of the Earth and Planetary Interiors* for peer review.

submitted to *Phys. Earth Planet. Inter.*

Robust estimates of the ratio between S- and P-wave velocity anomalies in the Earth's mantle using normal modes

Federica Restelli[1,†], Christophe Zaroli[2] & Paula Koelemeijer[1,3*]

[1] *Department of Earth Sciences, Queen's Building. Royal Holloway University of London, Egham Hill, Egham, Surrey, TW20 0EX, United Kingdom*

[2] *Institut Terre et Environnement de Strasbourg, UMR 7063, Université de Strasbourg, EOST/CNRS, 67084 Strasbourg cedex, France*

[3] *Department of Earth Sciences, University of Oxford, South Parks Road, Oxford, OX1 3AN UK, United Kingdom*

† *Corresponding author. Email: federica.restelli.2019@live.rhul.ac.uk*

* *Email: paula.koelemeijer@earth.ox.ac.uk*

13 September 2023

SUMMARY

Seismic tomography allows us to image the interior of the Earth. In general, to determine the nature of seismic anomalies, constraints on more than one seismic parameter are required, for example both the shear-wave velocity v_s and the compressional-wave velocity v_p. However, to jointly interpret tomographic models of variations in v_s and v_p ($\mathrm{dln}v_s$ and $\mathrm{dln}v_p$, respectively) or their ratio R, it is essential for them to share the same local resolution. Most existing models do not provide resolution information, and thus cannot guarantee to honour this condition. In addition, uncertainties are typically not provided, making it difficult to robustly interpret the ratio $R = \mathrm{dln}v_s/\mathrm{dln}v_p$. To overcome these issues, we utilise the recently developed SOLA tomographic method, a variant of the linear Backus–Gilbert inversion scheme. SOLA retrieves local-average model estimates, together with information on their uncertainties, whilst it also provides direct control on model resolution through target kernels. In this contribution, we apply SOLA to normal-mode data with sensitivity to both v_s and v_p, as well as density throughout the mantle. Specifically, we aim to develop models of both v_s and v_p with the same local resolution. We test our methodology and approach using synthetic tests for various noise cases (random noise, data noise or also additional *3D noise* due to variations in other physical parameters than the one of interest). We find that the addition of the 3D noise increases the uncertainties in our model estimates significantly, only allowing us to find model estimates in six or four layers for v_s and v_p, respectively. While the synthetic tests indicate that no satisfying density models can be obtained, we easily manage to construct models of $\mathrm{dln}v_s$ and $\mathrm{dln}v_p$ with almost identical resolution, from which the ratio R can be robustly inferred. The obtained values of R in our synthetic experiments significantly depend on the noise case considered and the method used to calculate it, with the addition of 3D noise always leading to an overestimate of R. When applying our approach to real data, we obtain values of R in the range of 2.5–4.0 in the lowest 600 km of the mantle, which are consistent with previous studies. Our model estimates with related resolving kernels and uncertainties can be used to test geodynamic model predictions to provide further insights into the temperature and composition of the mantle.

Key words: Free Oscillations; Seismic tomography; Composition and structure of the mantle; Uncertainties

1 INTRODUCTION

Seismic tomography is our most powerful tool for imaging the Earth's deep interior. However, the development of a tomography model is complicated by several factors that affect how robust the solution of the inverse problem is, such as the non-uniqueness of the solution (e.g. Nolet 2008), the heterogeneous data coverage (e.g. Zaroli et al. 2017), the chosen model parameterisation (Trampert & Snieder 1996), the noise in the data (e.g. Rawlinson et al. 2014). Given all these complications, a careful analysis of model resolution and covariance is fundamental to robustly interpret seismic images (e.g. Trampert 1998). Nonetheless, most global-scale tomographic models do not provide such uncertainty information, and the model robustness is not analyzed exhaustively (Rawlinson & Spakman 2016).

In the lowermost mantle in particular, the above issues concerning the robustness of tomography models prevent us from drawing conclusions about the nature of the observed seismic structures. Dozens of global tomography models exist, which consistently image two large antipodal regions of low seismic velocities (Large Low Velocity Provinces, LLVPs for short) underneath Africa and the Pacific. These have primarily been observed in shear-wave velocity (v_s) models (Lekić et al. 2012; Cottaar & Lekic 2016), but more recently also in compressional-wave velocity (v_p) models (Lekić et al. 2012; Koelemeijer et al. 2016; Garnero et al. 2016; Koelemeijer 2021), although the small-scale details and amplitudes do vary between models. Despite this consistent imaging of the LLVPs (at least on longer wavelengths), there are still several outstanding questions. In particular, the amount and distribution of chemically distinct material in the LLVPs remains debated, which influences their mobility and evolution as well as the planform of mantle convection through time (e.g. Garnero et al. 2016; McNamara & Zhong 2005; Davies et al. 2015; McNamara 2019).

In order to constrain the origin of the low seismic velocities of the LLVPs, it is important to consider multiple elastic parameters and to robustly determine the relative amplitudes of their anomalies. Commonly, the ratio R between perturbations in v_s ($\mathrm{dln}v_s$) and v_p ($\mathrm{dln}v_p$) is considered in studies of the lowermost mantle. Mineral physics experiments indicate that the ratio R in the LLVPs should be up to 2.5 if the low velocities are only due to thermal variations (Karato 1993; Karato & Karki 2001). Values greater than 2.5 imply the presence of either chemical heterogeneity (e.g. Su & Dziewonski 1997; Masters et al. 2000a) or the phase transition from bridgmanite to post perovskite (e.g. Oganov & Ono 2004; Koelemeijer et al. 2018). Robust information on R thus helps to distinguish between different physical interpretations of seismic anomalies.

In order to interpret a pair of v_s and v_p tomography models jointly, it is vital for them to have the same local resolution (Tesoniero et al. 2016). This can be problematic as traditional tomographic approaches do not allow a direct control on the model resolution, which thus prevents one to develop $\mathrm{dln}v_s$ and $\mathrm{dln}v_p$ models with identical local resolution. Moreover, the uncertainties associated with the perturbations, and therefore with the ratio R, are often not computed. Despite these issues, many studies have focused on obtaining and interpreting the ratio of seismic velocities (e.g. Su & Dziewonski 1997; Ishii & Tromp 1999; Masters et al. 2000a; Romanowicz 2001; Della Mora et al. 2011; Koelemeijer et al. 2016). These studies typically find ratios close to 1–1.5

in the upper mantle, and an increase in the ratio up to values larger than 2.5 in the lower mantle, an observation that has often been interpreted to imply chemical heterogeneity. However, without information on the v_s and v_p model resolution, it is difficult to assess whether the computed ratios, and hence their interpretation are robust.

In this study, we aim to solve these issues by developing mantle tomography models that are accompanied by uncertainty and resolution information. We strive to have the same resolution for v_s and v_p, so that their perturbations can be jointly interpreted in a robust way. To solve the inverse problem, we shall use the *Subtractive Optimally Localized Averages* (SOLA) method (Pijpers & Thompson 1992, 1994), a slight variant of the linear Backus-Gilbert (B–G) inversion scheme (Backus & Gilbert 1967, 1968, 1970). The SOLA method has been introduced and adapted to solve (large-scale) tomographic problems by Zaroli (2016, 2019). Contrary to the original B–G approach, SOLA allows for a direct control on the model resolution, which allows us to build $\mathrm{dln}v_s$ and $\mathrm{dln}v_p$ models with the same pre-specified resolution. This control on resolution and the availability of model uncertainties make it possible to analyse the robustness of $\mathrm{dln}v_s$ and $\mathrm{dln}v_p$ model estimates and to analyse to what extent we can interpret estimates of R. We apply the SOLA tomographic method to observations of normal mode splitting, thus focusing on the long wavelength structure of the mantle. The use of normal mode data has several advantages: they are directly sensitive to both shear- and compressional-wave velocities as well as density, they are sensitive to different depths spanning the whole mantle, and they provide a global data coverage.

This manuscript is structured as follows. In Section 2 we briefly summarise some important aspects of normal modes and introduce splitting function measurements. In Section 3 we present theoretical aspects of the SOLA method and discuss how we apply this to the normal mode data. In particular, we discuss methodological aspects such as the model parameterisation, inversion strategy and crustal corrections. Throughout Section 4 we detail the set-up and procedure for synthetic tests and present the corresponding results. We show the ability of normal modes to recover the input structure of an existing tomographic model, in terms of shear- and compressional-wave velocity perturbations. We also discuss the influence of different noise levels and the recovery of density anomalies in synthetic tests. Then, in Section 5 we perform inversions of observed splitting functions for v_s and v_p perturbations, also computing and discussing their ratio R. Finally, the discussion in Section 6 covers different topics such as the importance of estimating the noise accurately, the advantages and limitations of our approach and implications for both existing and future normal mode studies.

2 NORMAL MODES

Seismic recordings of normal modes (spectra) can be directly inverted for Earth structure (one-step inversion) or in two separate steps with splitting functions obtained as an intermediate step (two-steps inversion) (e.g. Li et al. 1991). The one-step inversion is non-linear and requires large amounts of computation time, which consequently only few studies have used (e.g. Li et al. 1991; Durek & Romanowicz 1999; Kuo & Romanowicz 2002). Instead, splitting functions are linearly related to 3D Earth structure and once a database of splitting functions is developed, it can be utilised repeatedly (Ishii & Tromp 1999; Mosca et al. 2012; Koelemeijer et al. 2016; Moulik & Ekström 2016, e.g.). While the use of splitting functions for studies of density has been questioned (Al-Attar et al. 2012; Akbarashrafi et al. 2017, e.g.), velocity models developed with the one-step or two-step inversion method are consistent with one another (Jagt & Deuss 2021). Here, we make use of splitting functions for our inverse problem, as SOLA is only applicable to linear problems.

2.1 Normal mode theory

Free oscillations or normal modes of the Earth arise after large earthquakes (typically with moment magnitude $M_w > 7.4$), when the Earth resonates like a bell. Due to the finite size of the Earth, only discrete resonance frequencies are permitted. Two different types of normal modes exist: (i) spheroidal modes, which involve vertical and horizontal motion, and (ii) toroidal modes, which involve horizontal motions only. Spheroidal mode multiplets ${}_nS_l$ and toroidal mode multiplets ${}_nT_l$ are characterised by their radial order n and angular order l. Each multiplet consists of $2l + 1$ singlets with azimuthal order m.

For a spherically symmetric, non-rotating, perfectly elastic and isotropic (SNREI) Earth model, all $2l + 1$ singlets of a given mode are degenerate, i.e. have the same frequency. Earth's rotation, ellipticity and aspherical structure – including topography on internal boundaries and lateral variations in isotropic and anisotropic structure – remove this degeneracy, resulting in so-called splitting of the multiplet. In the real Earth, normal modes may also exchange energy ("coupling"), but the "self-coupling" approximation (which consider multiplets in isolation) is commonly used in tomographic applications.

The splitting of a given mode is conveniently described by splitting function coefficients, introduced by Woodhouse et al. (1986). Using perturbation theory, these coefficients, denoted as c_{st}, are linearly related to the perturbations of the reference Earth model in shear-wave velocity ($\mathrm{dln}v_s$), compressional-wave velocity ($\mathrm{dln}v_p$), density ($\mathrm{dln}\rho$) and topography on internal boundaries ($\mathrm{dln}h$) as follows:

$$c_{st} = \int_0^a \left[\mathrm{dln}v_s(r)_{st} K_s^s(r) + \mathrm{dln}v_p(r)_{st} K_s^p(r) + \mathrm{dln}\rho(r)_{st} K_s^\rho(r)\right] dr + \sum_d \mathrm{dln}h_{st}^d H_s^d \quad (1)$$

where s and t indicate the spherical harmonic degree s and order t describing lateral heterogeneity in the Earth. $K_s^s(r)$, $K_s^p(r)$, $K_s^\rho(r)$ and H_s^d are the sensitivity kernels at degree s associated with the perturbations in v_s, v_p, density and topography of discontinuities, computed here using the 1D PREM model (Dziewonski & Anderson 1981). We focus here only on volumetric heterogeneity, thus neglecting the interface topography effects with the exception of the crust (see Section 3.5).

[Fig. 1 about here.]

Fig. 1 shows examples of sensitivity kernels at degree 2 for a few spheroidal modes. Since the sensitivity to v_s and ρ depends on the harmonic degree, sensitivity kernels at degrees 2, 4, 6 and 8 are shown in Supplementary Fig. S1. While some normal modes have targeted sensitivity to the shallow mantle (e.g. fundamental modes with $n = 0$ and high angular order l, Fig. 1a) or lowermost mantle (e.g. Stoneley modes, Fig. 1b), others have very oscillatory sensitivity, particularly in the mid mantle. As SOLA constructs resolving kernels by combining data sensitivity kernels, we can thus expect that it will be challenging to resolve structures in the mid mantle. Nevertheless, the fact that modes are sensitive to different parameters at different depths makes them suitable to study structures across the whole mantle.

2.2 Splitting function measurements

For the development of model SP12RTS, Koelemeijer et al. (2016) combined splitting function measurements that were obtained after 2011, including all v_p sensitive modes of Deuss et al. (2013) and the Stoneley modes of Koelemeijer et al. (2013). All measurements were obtained from the non-linear, iterative, least-squares inversion of seismic spectra (Deuss et al. 2013), using data from 93 earthquakes with $M_w > 7.4$ between 1976 and 2011. We use the same normal mode dataset as in model SP12RTS, given our main interest in both v_s and v_p perturbations and the focus on the lower mantle. However, we only use coefficients up to degree 8 as the number and quality of measurements above $s = 8$ drops significantly. Our dataset thus contains 143 spheroidal modes, with 5309 splitting function coefficients. We also exclude inner core sensitive modes, as in Koelemeijer et al. (2016), given our primary interest in mantle structure. Though some of the observed splitting functions were obtained using pair- or group-coupling, in this study we only consider the self-coupled parts of the splitting functions, limiting us to study even-degree heterogeneity only.

Uncertainties - including data uncertainties - play a crucial role in SOLA inversions. To determine the measurement uncertainties of the splitting functions in our dataset, a bootstrap resampling technique was used, as described in Deuss et al. (2013). This consists of remeasuring the splitting coefficients leaving out entire events at random in each inversion. The maximum range of measurements was taken for each coefficient to obtain a conservative estimate of measurement uncertainty. However, this procedure only considers uncertainties in the measurements due to the earthquake sources and data noise, while additional "theoretical errors" are also present (Resovsky & Ritzwoller 1998). Particularly, the error due to the use of the self- and group-coupling approximations can be considerable (Deuss & Woodhouse 2001; Al-Attar et al. 2012; Robson et al. 2022, e.g.) and it has been suggested that published measurement uncertainties should be multiplied by a factor of 2 to more accurately represent the true data uncertainties (Akbarashrafi et al. 2017).

3 METHODOLOGY

3.1 The SOLA-Backus-Gilbert method

The SOLA (Subtractive Optimally Localized Averages) method is an alternative formulation of the Backus–Gilbert (B–G) linear inversion scheme (Backus & Gilbert 1967, 1968, 1970), which retains all its advantages, but is more computationally efficient and versatile in the explicit construction of resolving kernels. The method was first developed for helio-seismic inversions by Pijpers & Thompson (1992, 1994) and introduced and adapted to seismic tomography by Zaroli (2016). For an exhaustive introduction to SOLA tomography, the reader is referred to Zaroli (2016) and Zaroli (2019) . Here, we only summarize the main points.

Inverse methods like SOLA, which belong to the Backus–Gilbert approach, do not seek to construct a particular model solution $\tilde{m}$, that is, to estimate infinitely many model parameters, but instead to determine some *optimally localized averages*, $\hat{m}$, over the 'true' model, m. This can be written in a general form as

$$\hat{m} = \int \hat{R} m \quad (+ \text{ propagated noise})\,. \tag{2}$$

The process of averaging, which is performed within a region represented by a resolving kernel $\hat{R}$, removes the non-uniqueness of the solution without the introduction of regularisation constraints on the model. Therefore, it is possible to identify unique averages, even when the (infinitely many) parameters themselves are not uniquely defined (Menke 1989).

While in the classic Backus–Gilbert formulation this resolving kernel $\hat{R}$ is designed to be as focused as possible, with SOLA we specify an *a priori* target form for $\hat{R}$, through the definition of a target (resolving) kernel T. The SOLA optimization problem then consists of seeking a local-average estimate $\hat{m}$ as a linear combination of the data, such that the resulting resolving kernel $\hat{R}$ is the closest possible to its target kernel T. At the same time, SOLA moderates the uncertainty, $\sigma_{\hat{m}}$, related to the model estimate, which represents in a statistical sense the propagation of noise into the model space. This can be summarised as follows:

$$\int (\hat{R} - T)^2 \,+\, \eta^2\, \sigma_{\hat{m}}^2 \,=\, min\,, \tag{3}$$

where η represents a trade-off parameter — the well-known trade-off between model resolution and model uncertainty (Backus & Gilbert 1970).

Specifying a target averaging kernel for every region of interest (within the model space) means that we have direct control on the local model resolution. We thus introduce *a priori* information on the model resolution, which is significantly different from assuming *a priori* information on the model itself (e.g. by using damping or smoothness constraints). We can also control the level of model uncertainty by varying the trade-off parameter. Moreover, both the resolving and target kernels are normalised to unity (i.e., $\int \hat{R} = \int T = 1$), so that we may obtain *unbiased* local averages with respect to the true model (e.g. Zaroli et al. 2017).

In summary, SOLA provides a direct control and valuable information on the model resolution and uncertainties, which are necessary to draw well-informed conclusions from tomographic images. The availability of both resolution and uncertainties (in addition to an ensemble of local-average model estimates) is a luxury that most other tomographic schemes do not provide (at least for large-scale problems, often due to the high computational costs). Finally, the key advantage of SOLA tomography for our study is that it allows us to build models of $\mathrm{dln}v_s$ and $\mathrm{dln}v_p$ with (almost) identical resolution.

3.2 Model parameterisation and target kernels

Vertically, the model is subdivided into 96 layers using the original PREM parameterisation (Dziewonski & Anderson 1981), with layer thickness varying from about 20 km at the surface to about 40 km at the CMB. This fine layering allows us to capture the characteristics of the sensitivity kernels, and minimizes the error introduced with the discretisation. While this may appear very fine, it is important to note there is a clear distinction between the model parameterisation and the thickness of the target kernels and thus the vertical resolution of the model.

Laterally, the model is parameterised into spherical harmonics up to degree 8, which gives a lateral resolution of about 5400 km at the surface and 2700 km at the CMB. The lateral parameterisation in spherical harmonics allows us to perform purely 1D (depth) inversions considering one spherical harmonic coefficient with degree s and order t at a time. The 3D model estimate and the associated uncertainties are then obtained by combining the results for different coefficients.

With 1D (depth) inversions, we only have to define 1D target kernels. Following Masters et al. (2000b) and Masters & Gubbins (2003), we choose the target kernels to be in the shape of a boxcar. Alternatively, we could have assumed smooth functions such as splines, to mimic the sensitivity kernels of the modes. However, our choice of boxcars simplifies the interpretation of the local averages, which can now be interpreted as the mean of the model between two depths (assuming that the obtained resolving kernels also approximate a boxcar).

Typically, when using body-wave or surface-wave data in 3D inversions, the size of the target kernels is guided by the heterogeneous data coverage and the local resolving length that could potentially be expected based on the ray density (e.g. Zaroli 2016, 2019; Latallerie et al. 2022). Since we perform 1D inversions using normal mode data, which provide global data coverage, we instead estimate the optimal thickness of the target kernels with synthetic tests, as explained further in Section 4.

3.3 Resolution misfit

To combine 1D model solutions at different spherical harmonic degree s and order t, it is vital that they all have the same local resolution, i.e. the resolving kernels are the same. To achieve this, we define the same target kernels for all degrees s, and we aim to obtain resolving kernels that fit these target kernels equally well for every spherical harmonic degree s (the kernels do not depend on order t). To quantify the similarity between target kernels and resolving kernels, we introduce the concept of resolution misfit (*RM*), defined as:

$$\textit{RM} = \frac{\int (\hat{R} - T)^2 \mathrm{dr}}{\int T^2 \mathrm{dr}}. \tag{4}$$

The smaller RM, the higher the fit between the resolving and target kernels. When building a 3D model, we want to ensure that *RM* is the same for the resolving kernels of all coefficients.

The trade-off parameter η now plays a fundamental role as changes in η lead to different *RM* values. To build a 3D tomographic model, we first of all choose a value of *RM* that provides the desired similarity between resolving and target kernels. Subsequently, we run a large number of inversions for each spherical harmonic degree while varying η until we obtain the desired value of *RM*. Fig. 2 presents an example of how this works in practice. We typically obtain similar, but different curves for different spherical harmonic degrees and thus select slightly different values of η for each degree to build the 3D tomographic model. Also note that *RM* values increase (worse resolution) for high η values while uncertainties decrease, in agreement with the expected trade-off between resolution and uncertainties.

[Fig. 2 about here.]

3.4 3D noise

Normal modes are simultaneously sensitive to multiple physical parameters, as is evident from Equation 1. Traditionally, this additional sensitivity is taken into account using scaling factors, e.g. the sensitivity to v_p and ρ are scaled and added to the sensitivity of v_s when inverting for v_s (e.g. Ritsema et al. 1999, 2011; Moulik & Ekström 2014). We do not want to take this approach since we do not want to assume any *a priori* information on the model parameters. Instead, we follow an approach similar to the one introduced by Masters (1979) (see also Masters & Gubbins 2003), where the effect of perturbations that are not of interest is seen as additional noise. We call this the "3D noise" (σ_{3D}), as it arises from the 3D structure of the Earth. For example, when inverting for perturbations in v_s, we need to take the contributions from v_p (C_{v_p}) and density (C_ρ) variations into account in the noise according to:

$$\sigma_{3D,v_s} = \sqrt{C_{v_p}^2 + C_\rho^2}. \tag{5}$$

Here, we estimate the 3D noise due to mantle structure by calculating splitting function predictions for 16 existing tomography models. A list of these models is given in Supplementary Table S1. To evaluate the 3D noise due to a particular physical parameter, we compute the splitting function coefficients using only perturbations in that parameter present in the mantle, with all other perturbations set to zero. For models that only constrain $\mathrm{dln}v_s$, we use the same $\mathrm{dln}v_p-\mathrm{dln}v_s$ and $\mathrm{dln}\rho-\mathrm{dln}v_s$ scaling relationships as used in the construction of the models, if these are known.

If not specified, we use a scaling factor of 0.5 for $\mathrm{dln}v_p - \mathrm{dln}v_s$ and 0.3 for $\mathrm{dln}\rho - \mathrm{dln}v_s$. For each normal mode and each coefficient s, t, we use the largest predicted value as 3D noise level, in order to estimate the noise in a conservative way. The total noise (σ_{tot}) is then given by adding the 3D noise to the data noise (σ_d):

$$\sigma_{tot} = \sqrt{\sigma_d^2 + \sigma_{3D}^2}. \tag{6}$$

Using this procedure, we typically find that the 3D noise for v_s is lower than the 3D noise for v_p and ρ, which have similar noise levels for most modes (Fig. 3). The measurement (data noise) levels are even lower in general.

[Fig. 3 about here.]

3.5 Crustal corrections

Accurate crustal corrections are required to avoid mapping crustal features into mantle structure during tomographic inversions. These corrections consist of both corrections for crustal velocities and topography on crustal interfaces. The effect of crustal velocities is typically neglected in the case of normal modes, as the thickness of the crust is a fraction of the wavelength of the data. We have verified that 3D variations in crustal velocities only change normal mode splitting functions by $< 0.5\%$ compared to the effect of variations in crustal topography, consistent with work by Moulik & Ekström (2014). Therefore, we neglect these volumetric variations, and only correct the data for topography on crustal interfaces, including the surface topography, water depth and Moho depth.

While surface topography and water depth can safely be assumed to be known, Moho depth variations have larger uncertainties. Restelli et al. (2023) demonstrated that predictions for normal modes sensitive to the lowermost mantle are not affected by the use of different crustal models. However, we want to verify that the way we account for the crust does not influence the results significantly in any part of the mantle. We have therefore performed additional synthetic tests during which we either consider the Moho depth to be known – and correct for it using model CRUST5.1 (Mooney et al. 1998) – or as unknown – and we include it in the 3D noise . In both cases, we find similar patterns in our model estimates with the difference in amplitudes less than

5% (Supplementary Fig. S2). Given the small difference between the two, for simplicity we assume the Moho depth to be known and correct for it using model CRUST5.1, in addition to correcting for surface topography and water level.

4 SYNTHETIC INVERSIONS

While the SOLA method has already been applied to body waves (e.g. Zaroli 2016, 2019), surface waves (Latallerie et al. 2022) and normal modes and body waves together (Dubois 2020), here we apply SOLA for the first time to normal modes only. The main difference in inversion setup between these studies and ours is that our data and model are parameterised in spherical harmonics, which allow us to perform pure 1D inversions in depth rather than in a 3D space. Rather than applying our inversion strategy directly to observed normal mode splitting functions, we first test our newly developed inversion strategy using synthetic experiments. Using these experiments we (i) verify that our implementation of SOLA allows us to recover a given input model, (ii) establish at what resolution normal modes are able to recover v_s, v_p and density structure in the mantle, (iii) study the trade-off between data noise levels and resolution (minimum averaging thickness) as a function of spherical harmonic degree, (iv) investigate different noise levels and the influence of 3D noise, (v) find the ideal value of the resolution misfit RM and, finally, (vi) we assess to what degree we should trust the model based on observed data.

4.1 Noise cases and input model

Since uncertainties play a fundamental role in SOLA inversions, we consider three cases with different levels of noise: we either only consider the published splitting function uncertainties (case DATA-N), or we replace these by random noise up to the same maximum amplitude as the data noise (case RAND-N), or we also consider 3D noise due to mantle structure in addition to the data noise (as in Eq. 6; case 3D-N). The noise levels in the random noise case are typically larger than for DATA-N since most of the coefficients have uncertainties lower than the maximum value.

As Akbarashrafi et al. (2017) suggested and mentioned before, we multiply the data uncertainties by a factor of 2 in the DATA-N and 3D-N cases, in order not to underestimate the data errors.

In the 3D-N case we also double the 3D noise amplitudes, to account for the fact that our estimates of 3D noise are based on tomography models predictions, whose amplitudes are typically halved due to damping and reparameterisations during the tomographic inversion (e.g. Schuberth et al. 2009; Koelemeijer et al. 2018). Thus, in the 3D-N case both noise contributions are multiplied by a factor of 2. The three cases can be summarised as follows:

$$\sigma = \begin{cases} 2 \times \sigma_d & \text{in DATA-N} \\ rand(0 - max(\sigma_d)) & \text{in RAND-N} \\ 2 \times \sqrt{\sigma_d^2 + \sigma_{3D}^2} & \text{in 3D-N} \end{cases} \tag{7}$$

To describe the 3D structure in the mantle and calculate synthetic splitting functions, we make use of model S20RTS (Ritsema et al. 1999). This model prescribes the v_s perturbations, while it makes use of scaling factors of 0.5 and 0.3 to prescribe perturbations in v_p and density, respectively. We compute synthetic splitting function predictions from S20RTS including all perturbations in v_s, v_p and density. For the DATA-N and RAND-N cases, we then assume the same scaling factors during the inversion, as commonly done in normal mode inversions. In contrast, in the 3D-N case we do not assume to know anything about the mantle structure and account for the additional sensitivity through the 3D noise.

4.2 Inversion procedure

We adopt the following procedure. Given our primary interest in the deep mantle, and the fact that SOLA allows us to target a specific depth range, we build a model from the bottom up, starting at the core-mantle boundary (CMB). We use an initial thick target kernel of about 1000 km thick (similar to the depth layers in early normal-mode based studies (Trampert et al. 2004)). We run SOLA inversions for spherical harmonic degree $s = 2$ for different values of η and choose a resolution misfit value that leads to an acceptable compromise between resolution and uncertainties, finding that $RM \sim 0.08$ is suitable. We then run inversions for similar ranges of η for all coefficients to find those η values that lead to the same RM of 0.8 (by trial and error). Having done this for all even-degree coefficients up to $s = 8$, we build the full model estimate combing the spherical harmonic coefficients. If the results are acceptable in terms of similarity between output and input models, resolution and uncertainties, we repeat the procedure for thinner and thinner target kernels (which will result in higher model uncertainties). Once we have obtained the thinnest possible target kernel that leads to uncertainties in a chosen range, we proceed to the next layer, repeating the procedure up to the surface.

To decide whether a model estimate is acceptable, we compare the model estimate (output model) with the "filtered" input model, i.e. the input model averaged through the same resolving kernels as the output. This ensures we are comparing the same average, which is justified by the fact that we are interested in finding a weighted average of the models parameters, not the parameters themselves. To quantify how acceptable the uncertainties are, we will use a "relative uncertainty", which is the model average uncertainty divided by the maximum model amplitude. We aim to have a relative uncertainty of 20–25$\%$ for σ_{v_s} and $< 50\%$ for σ_{v_p}, similar to the uncertainty levels found by Mosca et al. (2012). We then define the output model amplitudes "unbiased" if we can recover the filtered input model amplitudes within the model uncertainties.

4.3 S-wave velocity structure from synthetic experiments

We start our synthetic experiments by performing inversions for shear-wave velocity perturbations, as the v_s perturbations in the mantle have the highest amplitudes and the lowest 3D noise, and are thus likely the easiest ones to recover. We apply the procedure described above to cases DATA-N and RAND-N (results shown in Supplementary Fig. S3 and S4) as well as case 3D-N (with results shown in Fig. 4). By comparing the three cases, we can investigate the influence and importance of the different uncertainties.

[Fig. 4 about here.]

Following the procedure in Section 4.2, we are able to obtain model estimates with acceptable resolving kernels throughout the mantle, while able to keep the relative uncertainty below 25$\%$ in every layer. In the DATA-N and RAND-N case, we would be able to invert for more layers, but to ensure that we can directly compare the results of different noise cases, we limit the number of layers in these case to the maximum number of layers we are able to obtain in the 3D-N case, i.e. six. These six layers vary in thickness from ∼220 km at the surface to ∼350 km at the CMB, with very thick layers (resolving kernels) of ∼820 km in the mid mantle. For the DATA-N and RAND-N cases shown in Supplementary Fig. S3 and S4 respectively, in each layer the output model estimate closely resembles the filtered input model, and we recover both the amplitudes and the pattern of the anomalies well. The associated model uncertainties are typically $< 15.5\%$.

For the 3D-N case (shown in Fig. 4) we still obtain very similar model estimates, but with higher model uncertainties (between 17 and 25%) as expected. Even in layers in the mid mantle (e.g. layers ULM and LLM, where output model amplitudes are overestimated), the difference between the filtered input and output is smaller than the uncertainties. This makes our model estimate an unbiased average of the input model given these uncertainties. Except for the increase in the uncertainties, the inclusion of 3D noise does not lead to significant differences to the DATA-N or RAND-N cases. We conclude that the sensitivity of the normal modes to v_p and density perturbations, which affects our inversions through the 3D noise, mainly has an effect on the noise propagated into the model, and not on the recovered $\mathrm{dln}v_s$ model estimate itself.

4.4 P-wave velocity mantle structure from synthetic experiments

Given the higher levels of 3D noise and lower amplitudes of $\mathrm{dln}v_p$ in the mantle, we expect that v_p models are more difficult to build than v_s models. Consequently, we do not anticipate obtaining the same resolution as for $\mathrm{dln}v_s$. We again apply our procedure (Section 4.2) to all three noise cases when inverting for $\mathrm{dln}v_p$, with results for the DATA-N and RAND-N cases shown in Supplementary Fig. S5 and S6, respectively, and the results for the 3D-N case presented in Fig. 5.

We are able to build v_p model estimates with satisfying resolving kernels and uncertainties in four layers in the mantle, which vary in thickness from ∼600 km at the CMB to ∼1000 km in the mid mantle. The results for cases DATA-N and RAND-N (Fig. S5 and S6) are satisfactory in all four layers: the output model estimates closely resemble the filtered input model and uncertainties are well below the threshold. When adding 3D noise in case 3D-N (Fig. 5), the results are not as positive. Only in the lowermost mantle (layer LLM), we are able to obtain model estimates that resemble the filtered input with a relative uncertainty of about 31% and unbiased amplitudes, implying that we are able to constrain the v_p structure in the lowermost mantle within our setup.

In the other three layers, the output model estimates still feature positive and negative anomalies in similar locations as the input models, but their amplitudes and uncertainties are less satisfying. Especially, for the upper mantle layer (layer UM) the model estimate is biased towards high amplitudes with a large discrepancy between the filtered input and model output. The two layers in the mid mantle have quite high relative uncertainties, which are close to 50% (our threshold), but similar to the uncertainty amplitudes found in older work (Mosca et al. 2012). Contrary to the inversions for $\mathrm{dln}v_s$, the sensitivity to other physical parameters (especially v_s) as quantified in the 3D noise affects both the model uncertainties and the recovered v_p structure.

[Fig. 5 about here.]

4.5 $\mathrm{dln}v_s/\mathrm{dln}v_p$ from synthetic experiments

When comparing maps of $\mathrm{dln}v_s$ and $\mathrm{dln}v_p$, it is vital for them to have the same local resolution, as discussed in the Introduction. It is therefore not our aim to develop models with the best resolution achievable, but instead to end up with models of $\mathrm{dln}v_s$ and $\mathrm{dln}v_p$ with the same local resolution. From our synthetic tests above, we have found that the resolution of $\mathrm{dln}v_p$ models is lower than that of $\mathrm{dln}v_s$ models. Consequently, the $\mathrm{dln}v_p$ resolution will dictate the maximum resolution that we may expect to obtain for the $\mathrm{dln}v_s/\mathrm{dln}v_p$ ratio. Given the larger uncertainties for $\mathrm{dln}v_p$ models in the mid mantle, we focus our efforts only on the lowest layer, i.e. the bottom ~600 km of the mantle, where we managed to obtain satisfying results for $\mathrm{dln}v_p$ (relatively low uncertainties and unbiased amplitudes) and the depth region of interest in the debate surrounding the LLVPs. To obtain the same local resolution for v_s as v_p, we repeat SOLA inversions for $\mathrm{dln}v_s$ using the same target kernel thickness as in layer LLM of the $\mathrm{dln}v_p$ model. For each coefficient, we vary the trade-off parameter η until we obtain the same resolution misfit RM as for $\mathrm{dln}v_p$ ($RM \sim 0.08$). This way we ensure that the resolving kernels, and hence the local resolution, are comparable for the $\mathrm{dln}v_s$ and $\mathrm{dln}v_p$ models (e.g. Fig. 6a).

Computing the $\mathrm{dln}v_s/\mathrm{dln}v_p$ ratio in a tomographic model can be tricky, as we may be dividing by small numbers (small v_p anomalies) and previous studies have taken several different approaches. The most straightforward way may be by performing a point-by-point division and considering the median or mean (from now on "pbp division"), but studies have also calculated the root-mean-squares average of both velocities and divided these values (from now on "RMS division"), or determined the slope of the best fitting straight line between $\mathrm{dln}v_p$ and $\mathrm{dln}v_s$ values (from now on "regression fit method"). While the latter approach tends to provide an overestimation of R, the median of a pbp division often represents an underestimate (e.g. Koelemeijer et al. 2016). Here, we explore all three approaches.

Specifically, we always assume that our SOLA model estimates of $\mathrm{dln}v_s$ and $\mathrm{dln}v_p$ are two normally-distributed variables. In the pbp and RMS ratio estimates, we assume for simplicity that the two variables are independent, and we calculate the ratio distribution respectively for each point of a 5×5 degrees grid, while we do not have to make this assumption for the regression fit method. When performing the point-by-point division, we discard points with either $|\mathrm{dln}v_s| < 0.1\%$ or $|\mathrm{dln}v_p| < 0.1\%$ to avoid spurious R estimates, similar to Koelemeijer et al. (2016). Although we could approximate the ratio distribution (Hinkley ratio distribution) to a Gaussian distribution and express R in terms of a mean and standard deviation, this is often not possible. Therefore, we only report the mean value of R here without the uncertainties. However, thanks to the synthetic experiments, where we know what the value of R should be, we get an insight into how much R is biased with each method.

Since v_p perturbations in S20RTS are scaled from v_s perturbations with a factor of 0.5, the ratio R that we retrieve in our synthetic experiments should be exactly 2. Our results for R in the LLM layer are shown in Fig. 6 for each of the three noise cases analysed in this paper. We have chosen the colour scales in such a way that identical maps of v_s and v_p anomalies would indicate the expected ratio of 2. When we only include data noise or random noise (DATA-N and RAND-N in Fig. 6), the two maps are almost identical and the ratio assumes values very close to 2 regardless of the method used to calculate it. When we also consider 3D noise, we immediately note darker colours in the v_s map than the v_p map and thus a ratio greater than 2 with a broader distribution. In this 3D-N case, the ratio is overestimated by 20–40% depending on the method we use to evaluate it. While we do not observe any systematic bias in the pbp and RMS estimates of the ratio, we find that the regression fit gives an upper bound, consistent with earlier work (Koelemeijer et al. 2016).

[Fig. 6 about here.]

4.6 Density structure recovered in synthetic experiments

Besides constraining velocity variations, splitting function measurements have also been used in inversions for the mantle density (Ishii & Tromp 1999; Trampert et al. 2004; Mosca et al. 2012; Koelemeijer et al. 2017, e.g.). However, several studies have argued that the use of the self-coupling approximation introduces a theoretical error that is larger than the signal of mantle density in the data (Deuss & Woodhouse 2001; Al-Attar et al. 2012; Akbarashrafi et al. 2017), which is why we doubled the data noise in our SOLA inversions. Additional uncertainties in mid mantle structure further affect density inversions (Koelemeijer et al. 2017; Robson et al. 2022), an effect that we capture in the 3D noise. SOLA thus allows us to investigate whether it is possible, given these complications, to construct an acceptable resolving kernel and a model estimate with acceptable uncertainties for density at the base of the mantle.

We again perform synthetic tests with and without 3D noise, now for a $\sim$1000 km thick target kernel at the bottom of the mantle, with the results shown in Fig. 7. We manage to obtain resolving kernels with a low resolution misfit (i.e. reproduce the target kernel well) for all coefficients, meaning that there is sufficient sensitivity to density in the data set. When we only use data noise or random noise (Fig. 7 top and middle row), we retrieve the input model well, including the amplitudes and with relative uncertainties of about 4%. This would be similar to studies that inverted for density while keeping the velocity structure fixed. However, when we include the 3D noise, the recovered amplitudes are strongly overestimated and the relative uncertainty is close to 70%. This indicates that inversions for density are mostly complicated by unconstrained structure in the rest of the mantle, consistent with other recent work (Robson et al. 2022). Nevertheless, in our synthetic case, we would be able to interpret the LLVPs as low density anomalies despite this, given the strong negative anomalies found at their locations ($\mathrm{dln}\rho \sim -1.47\%$ with $\sigma_\rho \sim 1.03$).

[Fig. 7 about here.]

5 REAL DATA INVERSIONS FOR MANTLE STRUCTURE

In the following sections, we show the results from inversions using observed splitting functions (Deuss et al. 2013; Koelemeijer et al. 2013; Koelemeijer 2014). The setup of these real data inversions is guided by our synthetic tests and we use the same target kernels (6 for v_s and 4 for v_p), which will aid in drawing conclusions from our study. 3D noise is included as described in Section 3.4, making the real data inversions most comparable to the 3D-N case. We present model estimates of v_s, v_p and R, all depicting lateral variations with respect to PREM, together with relevant resolution and uncertainty information. We compare our results to two other tomography models that use normal modes, filtered using our resolving kernels. Specifically, we consider model SP12RTS, since we use the same normal mode data set and this model constrained both v_s and v_p perturbations, as well as model S20RTS, which we use for our synthetic tests, but included fewer and older measurements.

5.1 Model estimates of S-wave velocity perturbations

Fig 8 presents our results from real data inversions for $\mathrm{dln}v_s$ in the six-layer setup of the synthetic tests. We can observe many features common in long-wavelength tomography models. At shallow depths (layer UUM), we identify low velocity zones at locations of mid-ocean ridges and high velocities underneath cratons and in the proximity of subduction zones. At greater depth, particularly in the ULM layer, we find fast velocities at areas of deep subduction under South America and South-East Asia. In the deepest two layers, we observe low velocities under the Pacific and Africa, with the amplitudes of these LLVPs increasing towards the bottom of the mantle.

Compared to the other two models, we find stronger amplitudes in our model estimates, particularly when we compare to model SP12RTS (which utilised the same normal mode dataset). Nevertheless, we do not identify significant differences between our results and the other models, as expected given the large consistency between long-wavelength tomographic models (e.g. Lekić et al. 2012; Koelemeijer 2021). However, our model estimates have additional information on the resolution and the model uncertainties, which these older models do not. Specifically, we note that typically find a low relative uncertainty for our v_s model estimates, ranging from 15-19% in the upper mantle, increasing to 31% in the mid mantle and decreasing again below 2000 km to 23-24%. The mid mantle thus remains the least constrained part of our model, but at least we can quantify how unconstrained it is.

[Fig. 8 about here.]

5.2 Model estimates of P-wave velocity perturbations

Fig. 9 shows the results for our real data inversions for $\mathrm{dln}v_p$ compared to SP12RTS and S20RTS, using the same four target kernels as in our synthetic tests. While we do show results for the first layer (UM), we do not interpret them (greyed out) as the results in the synthetic tests at these depths were biased towards higher amplitudes, despite their low relative uncertainties. In the mid mantle, we observe two areas of higher velocities underneath South America and Southeast Asia – similar as in the v_s model – consistent with regions where deep subduction is thought to occur. In the lowest two layers, we again find low velocities underneath Africa and the Pacific, with the amplitudes increasing slightly towards the CMB.

In general, there is less consensus on the compressional-wave velocity structure of the mantle, and even though many models feature LLVPs, there is more variability in terms of shape, length-scales, location and velocity amplitudes. The LLVP structures in our v_p model estimate are similar to those in SP12RTS and S20RTS, but our model features typically higher amplitudes than in SP12RTS and lower amplitudes than in S20RTS (for both the negative anomalies in the LLVPs and the positive anomalies surrounding them). Although the absolute uncertainties appear relatively low, due to the low v_p amplitudes, the relative uncertainties are greater than 50% in the two mid mantle layers, and $\sim$42% in the lowermost mantle layer. Despite the uncertainties, we can still interpret v_p anomalies at the LLVPs locations as lower than average.

[Fig. 9 about here.]

5.3 Model estimates of the ratio R in the lowermost mantle

To constrain the ratio R in the mantle, it is essential that our model estimates of shear-wave and compressional-wave velocity have the same resolution, as discussed in Section 4.5. Therefore, we have obtained model estimates for v_s perturbations using the same target kernel as used for v_p and we impose the same resolution misfit value to obtain similar-shaped resolving kernels.

[Fig. 10 about here.]

In Fig. 10 we show our results from real data inversions for the ratio R as an average in the bottom 600 km of the mantle. The amplitudes in the v_s map are markedly higher than those in the v_p map (which has a color scale that is half the amplitude), so it already appears visually that the ratio must be larger than 2. When calculating the ratio using three different methods, we find R values of 3.7, 2.9 and 5.6 for R_{pbp}, R_{rms} and R_{fit} respectively. However, from the synthetic experiments, we know that the ratio can be overestimated by up to 40% depending on the method used to calculate it. Assuming that this overestimation is linear, the R values in our model may be reduced to 2.9, 2.5 and 4.0 for the pbp division, the RMS division and the regression-fit method, respectively. As caveat, we should add that the regression-fit method may be affected by small values and tends to overpredict the value of R. Thus, depending on the method to calculate it, the R value may be as low as 2.5, the value compatible with a mantle without compositional heterogeneity or phase transitions. Therefore, we should avoid interpreting our results as being indicative of a high $\mathrm{dln}v_s/\mathrm{dln}v_p$ ratio.

Results for all four layers (associated with the resolving kernels in Fig. 9) indicate that the ratio R increases with depth in the mantle, despite the thick resolving kernels (Supplementary Fig. S7). This is in agreement with previous studies, which also reported increases in the ratio with depth up to values of 4 near the CMB (e.g. Su & Dziewonski 1997; Masters et al. 2000a; Ritsema & van Heijst 2002; Della Mora et al. 2011; Koelemeijer et al. 2016). The range of R values we find is thus consistent with these studies, with the main difference being that we are confident that the resolution of our v_s and v_p model estimates is comparable.

6 DISCUSSION

To accurately compute and robustly interpret ratios of seismic velocities (e.g. $R = \mathrm{dln}v_s/\mathrm{dln}v_p$), it is crucial to obtain models of $\mathrm{dln}v_s$ and $\mathrm{dln}v_p$ models with the same local resolution. This is challenging since most of the commonly-used inverse methods do not provide a direct control on model resolution. Moreover, model uncertainties are often not provided, making physical interpretations in terms of temperature and chemical variations difficult. We have overcome these issues by utilising the SOLA method and applying this to normal mode data in order to develop long-wavelength models of v_s and v_p perturbations as well as their ratio. We will now discuss some aspects of our study, including the importance of characterising the noise, the advantages and limitations of our approach, and some implications for existing and future inversions of normal mode data.

6.1 Characterising data noise

The entire SOLA philosophy and approach to constructing Earth models is highly dependent on the data noise. Therefore, it is crucial to accurately estimate data noise levels and to reduce these where possible. However, the uncertainties in our data set, calculated as explained in Deuss et al. (2013), do not take into account all the sources of uncertainty, including theoretical approximations (Resovsky & Ritzwoller 1998). Al-Attar et al. (2012) and Akbarashrafi et al. (2017) suggested that published splitting function uncertainties must be doubled to properly account for different sources of errors, which we have therefore assumed throughout this work. In fact, when we do not double the data noise, we do not recover the input structures (see Supplementary Fig. S8). Thus, at the moment our SOLA inversions require the data noise to be doubled.

Our normal mode splitting function observations are all measured using spectral data from very large earthquakes. Since earthquakes with magnitude greater than 7.4 are relatively rare, long-running reliable broadband networks are crucial to obtain these data and to reduce data uncertainties. The expansion of the global seismic network (GSN) in the last 20 years, together with the occurrence of large earthquakes such as the Tohoku event in 2011, has substantially improved normal mode measurements. Nowadays, the number of GSN stations able to resolve normal modes from large earthquakes is almost twice the number in 2014, thanks also to the installation of seismometers in boreholes and postholes (Ringler et al. 2022). These types of installations are less subject to non-seismic noise than surface installations, which will reduce the overall noise levels of low-frequency data. Having more and quieter long-period broadband instruments will ultimately lead to improved measurements and thus reduced measurement uncertainties.

In our synthetic inversions for v_p and density (see Section 4), we generally obtained satisfying resolving kernels with a low resolution misfit, indicating that there is sufficient sensitivity in our normal mode data set to these parameters. The fact that our model estimates were also satisfying (output resembling input with low uncertainties) for the DATA-N and RAND-N cases, but not for case 3D-N demonstrates that it is the sensitivity to other physical parameters (especially v_s) that prevents us from obtaining robust models of v_p and density throughout the mantle. This notion is consistent with other recent work on normal mode measurements and density inferences (e.g. Koelemeijer et al. 2017; Robson et al. 2022). Therefore, efforts should also focus on firstly developing long-wavelength models of the mantle with uncertainties and secondly reducing the uncertainties in these models. One possible approach to take, may be to utilise SOLA inversions to constrain v_s at first and use the model estimate including its uncertainties to estimate the 3D noise for v_p and subsequently density, iterating if necessary.

6.2 Advantages and limitations of our approach

The main advantage of SOLA is that it allows us to directly constrain the resolution of our model estimate, thus enabling us to build models of different physical parameters with the same local resolution and to robustly interpret these. This is particularly useful in studies of the $\mathrm{dln}v_s/\mathrm{dln}v_p$ ratio R, given it is possible that differences in resolution affect this parameter (e.g. Chaves et al. 2021). Our approach, of focusing on finding the worst resolution in one physical parameter and imposing this on inversions for other physical parameters is easily expandable to other data sets, where it should be kept in mind that it is only the local resolution that needs to be the same, and not necessarily the data set used for each parameter. As a result, we may not get the best possible resolution for every parameter, and finding the best possible target kernels and η values can be time consuming.

SOLA also allows us to retrieve models of the Earth with unbiased amplitudes and uncertainty information (e.g. Zaroli et al. 2017). Tomographically filtered geodynamic models of thermal or thermochemical convection in the mantle mostly differ in their amplitudes (e.g. Ritsema et al. 2007; Davies et al. 2012), making the availability of unbiased SOLA model estimates with uncertainties important for distinguishing between the two scenarios. Although the fact that we only recover satisfying model estimates for six or four layers may appear disappointing, it should be kept in mind the these model estimates represent true averages over the Earth thus provide valuable information. For example, they can be used to compare to geodynamic simulations with our resolving kernels acting as tomographic filter. Given that we also have the model uncertainties, we should be able to rule out filtered geodynamic models that do not fit our model estimates within their uncertainties. Improving both data and 3D noise estimates would allow us to recover the model in thinner layers and thus achieve a better local resolution for such comparisons, as evidenced by our results for the DATA-N and RAND-N cases.

Our study is entirely based on normal mode data. The advantage of this is that inversions are extremely quick (just a few seconds for each coefficient). This makes it possible to perform many synthetic inversions with various set-ups. On the down-side, our choice of data limits us to only image the large-scale and even-degree structure of the mantle. However, we believe that a robust characterisation of the long-wavelength structures remains essential before attempting to robustly image small-scale features. It will also be possible to add different data types (e.g. body and surface waves) to improve the sensitivity to particularly depths and to illuminate small-scale structures not observable with normal modes. It will also be interesting to see how comparable the results are when our approach is applied to body-wave data only in order to constrain R in the mantle.

Finally, our study relies on estimates of 3D noise, which significantly increases the uncertainties associated with our models. However, the 3D noise ensures that we do not assume any *a priori* knowledge about the final model and the relationship between different parameters. Here, we used existing tomographic models to estimate the 3D noise levels in a conservative way, as it is better to overestimate the noise and then later re-assess this. Alternatively, we could have made use of geodynamic model predictions, but these are affected by several, still uncertain, parameters such as the rate of internal heating and CMB temperature, as well as the mineral physics data used for the conversion from temperature to seismic velocities. Thus, we believe our approach of using a range of tomographic models to estimate the 3D noise is at current the best possible way we have.

6.3 Implications for existing and future normal mode studies

Splitting function measurements have been used in many tomographic studies of the mantle, to constrain not just the velocity structure, but also density variations. We have shown that we can develop satisfying model estimates of both the shear-wave and compressional-wave velocity in the mantle in at least a number of layers, with uncertainties of less than 32% and 50% (compared to around 55% and 70% in the study of Mosca et al. (2012). Over time, as data uncertainties decrease and consequently the uncertainties of our v_s and v_p model estimates decrease as well, we may be able to increase the number of layers in the mantle and re-evaluate our work on the density structure.

Our synthetic tests for density fail when 3D noise is included and we find large model uncertainties (Fig. 7, despite the fact that we are able to obtain resolving kernels with a low resolution misfit. This warrants us to be cautious of published density models of the mantle that have shown focused resolving kernels. Instead we need to emphasise the fact that a good resolution does not imply a low model uncertainty or the ability to interpret a model.

In this study, we have focused our studies on R, the ratio between shear-wave and compressional-wave velocity variations. However, our approach of finding the same local resolution for two physical parameters (here v_s and v_p) can be easily extended to other parameters. Particularly, it will be useful for developing models of anisotropy, as we can ensure that v_{sh} and v_{sv} have the same local resolution. In order to study anisotropy using SOLA applied to normal modes, good-quality measurements of toroidal modes are vital. We have recently demonstrated that current data sets of toroidal mode measurements (including the new measurements of Schneider & Deuss (2021)) contain sufficient sensitivity to both shear-wave and compressional-wave anisotropy in the mantle (Restelli et al. 2023). It will be interesting to see whether SOLA inversions applied to these data are able to constrain the anisotropic structure of the Earth's mantle.

CONCLUSIONS

In this contribution we have, for the first time, applied the tomographic SOLA inversion scheme (Zaroli 2016) to a dataset consisting of only normal modes. This has allowed us to build global tomography models of shear- and compressional-wave velocity in several layers in the mantle. These models are accompanied by full uncertainty and resolution information, which helps us to assess the robustness of the model estimates. Over time, as more precise measurements are available and with better constraints on overall mantle structure (i.e. improved estimates of both data and 3D noise), we may be able to constrain the v_s and v_p structure in thinner layers (i.e. achieve a better resolution) and decrease the uncertainties in our model estimates.

SOLA also provides a direct control on the model resolution. As a result, we have managed to construct models of $\mathrm{dln}v_s$ and $\mathrm{dln}v_p$ with the same local resolution, which enables us to robustly compute their ratio R. Our synthetic tests indicate that estimates of R are overestimated when additional 3D noise is included. When taking this into consideration, our estimates of R in the lowermost mantle from real data are 2.5–4.0. These values are consistent with previous studies, but the additional information on resolution and uncertainty will allow us to perform meaningful comparisons with geodynamics.

We have demonstrated the importance of estimating all sources of the data noise, given its strong impact on the model estimates and uncertainties. In particular, when normal mode studies do not account for "theoretical errors" due to coupling approximations, or treat the additional sensitivity to other physical parameters as known, it is likely that model uncertainties are underestimated. Given the results for density in our synthetic tests (satisfying resolving kernels, but model estimates with very large uncertainties), we urge readers to be careful with interpreting tomographic images based on normal modes when resolution and uncertainties are not both available.

Data availability

The Python/C software package to develop SOLA tomography models is available from CZ (c.zaroli@unistra.fr), upon reasonable e-mail request.

CRediT author statement

FR: Formal analysis, Data curation, Visualization, Writing–Original draft preparation. **CZ:** Conceptualization, Methodology, Software, Supervision, Writing–Reviewing and Editing. **PK:** Funding acquisition, Conceptualization, Methodology, Software, Project administration, Supervision, Writing–Reviewing and Editing.

Acknowledgements

FR received funding from Royal Society grants (RGF\EA\181029 and RF\ERE\210182) awarded to PK. FR also received financial support from SEDI to attend the 17th SEDI Symposium in Zurich (2022) and gratefully acknowledges their support. PK acknowledges financial support from a Royal Society University Research Fellowship (URF\R1\180377). CZ acknowledges the High Performance Computing Center of the University of Strasbourg for supporting this work by providing scientific support and access to computing resources. The authors also thank the members of the seismological society for making tomographic models and normal mode observations available. All figures were produced using the GMT software (Wessel et al. 2013).

REFERENCES

Akbarashrafi, F., Al-Attar, D., Deuss, A., Trampert, J., & Valentine, A., 2017. Exact free oscillation spectra, splitting functions and the resolvability of Earth's density structure, *Geophys. J. Int.* , **213**(1), 58–76.

Al-Attar, D., Woodhouse, J. H., & Deuss, A., 2012. Calculation of normal mode spectra in laterally heterogeneous earth models using an iterative direct solution method, *Geophysical Journal International*, **189**(2), 1038–1046.

Backus, G. & Gilbert, F., 1968. The resolving power of gross earth data, *Geophysical Journal International*, **16**(2), 169–205.

Backus, G. & Gilbert, F., 1970. Uniqueness in the inversion of inaccurate gross earth data, *Philosophical Transactions of the Royal Society of London. Series A, Mathematical and Physical Sciences*, **266**(1173), 123–192.

Backus, G. E. & Gilbert, J., 1967. Numerical applications of a formalism for geophysical inverse problems, *Geophysical Journal International*, **13**(1-3), 247–276.

Chaves, C. A., Ritsema, J., & Koelemeijer, P., 2021. Comparing ray-theoretical and finite-frequency teleseismic traveltimes: implications for constraining the ratio of s-wave to p-wave velocity variations in the lower mantle, *Geophysical Journal International*, **224**(3), 1540–1552.

Cottaar, S. & Lekic, V., 2016. Morphology of seismically slow lower-mantle structures, *Geophys. J. Int.* , **207**(2), 1122–1136.

Davies, D. R., Goes, S., Davies, J. H., Schuberth, B. S. A., Bunge, H., & Ritsema, J., 2012. Reconciling dynamic and seismic models of Earth's lower mantle: The dominant role of thermal heterogeneity, *Earth Planet. Sci. Lett.* , **353**, 253–269.

Davies, D. R., Goes, S., & Lau, H. C. P., 2015. Thermally Dominated Deep Mantle LLSVPs: A Review, in *The Earth's Heterogeneous Mantle*, pp. 441–477, eds Khan, A. & Deschamps, F., Springer International Publishing.

Della Mora, S., Boschi, L., Tackley, P., Nakagawa, T., & Giardini, D., 2011. Low seismic resolution cannot explain S/P decorrelation in the lower mantle, *Geophys. Res. Lett.* , **38**(12).

Deuss, A. & Woodhouse, J., 2001. Theoretical free-oscillation spectra: the importance of wide band coupling, *Geophys. J. Int.* , **146**(3), 833–842.

Deuss, A., Ritsema, J., & van Heijst, H.-J., 2013. A new catalogue of normal-mode splitting function measurements up to 10 mHz, *Geophys. J. Int.* , **192**(3), 920–937.

Dubois, F., 2020. Global mantle tomography using backus-gilbert inversion of normal-mode and finite-frequency s-wave data, *PhD thesis, University of Strasbourg*.

Durek, J. J. & Romanowicz, B., 1999. Inner core anisotropy inferred by direct inversion of normal mode spectra, *Geophysical Journal International*, **139**(3), 599–622.

Dziewonski, A. & Anderson, D., 1981. Preliminary reference Earth model, *Phys. Earth Planet. Inter.* , **25**(4), 297–356.

Garnero, E., McNamara, A., & Shim, S.-H., 2016. Continent-sized anomalous zones with low seismic velocity at the base of Earth's mantle, *Nature Geosci.* , **9**(7), 481–489.

Ishii, M. & Tromp, J., 1999. Normal-mode and free-air gravity constraints on lateral variations in velocity and density of Earth's mantle, *Science* , **285**(5431), 1231.

Jagt, L. & Deuss, A., 2021. Comparing one-step full-spectrum inversion with two-step splitting function inversion in normal mode tomography, *Geophysical Journal International*, **227**(1), 559–575.

Karato, S., 1993. Importance of anelasticity in the interpretation of seismic tomography, *Geophys. Res. Lett.* , **20**(15), 1623–1626.

Karato, S.-i. & Karki, B. B., 2001. Origin of lateral variation of seismic wave velocities and density in the deep mantle, *J. Geophys. Res.* , **106**(R10), 21771–21783.

Koelemeijer, P., 2021. Toward consistent seismological models of the core–mantle boundary landscape, *Mantle convection and surface expressions*, pp. 229–255.

Koelemeijer, P., Deuss, A., & Ritsema, J., 2013. Observations of core-mantle boundary Stoneley modes, *Geophys. Res. Lett.* , **40**(11), 2557–2561.

Koelemeijer, P., Ritsema, J., Deuss, A., & Van Heijst, H.-J., 2016. SP12RTS: a degree-12 model of shear- and compressional-wave velocity for Earth's mantle, *Geophys. J. Int.* , **204**(2), 1024–1039.

Koelemeijer, P., Deuss, A., & Ritsema, J., 2017. Density structure of Earth's lowermost mantle from Stoneley mode splitting observations, *Nature Comm.* , **8**, 15241.

Koelemeijer, P., Schuberth, B. S., Davies, D. R., Deuss, A., & Ritsema, J., 2018. Constraints on the presence of post-perovskite in Earth's lowermost mantle from tomographic-geodynamic model comparisons, *Earth Planet. Sci. Lett.* , **494**, 226–238.

Koelemeijer, P. J., 2014. Normal mode studies of long wavelength structures in Earth's lowermost mantle, *PhD thesis, University of Cambridge*.

Kuo, C. & Romanowicz, B., 2002. On the resolution of density anomalies in the Earth's mantle using spectral fitting of normal-mode data, *Geophys. J. Int.* , **150**(1), 162–179.

Latallerie, F., Zaroli, C., Lambotte, S., & Maggi, A., 2022. Analysis of tomographic models using resolution and uncertainties: a surface wave example from the pacific, *Geophysical Journal International*, **230**(2), 893–907.

Lekić, V., Cottaar, S., Dziewonski, A., & Romanowicz, B., 2012. Cluster analysis of global lower mantle tomography: A new class of structure and implications for chemical heterogeneity, *Earth Planet. Sci. Lett.* , **357**, 68–77.

Li, X., Giardini, D., & Woodhouses, J., 1991. Large-scale three-dimensional even-degree structure of the Earth from splitting of long-period normal modes, *J. Geophys. Res.* , **96**(B1), 551–577.

Masters, G., 1979. Observational constraints on the chemical and thermal structure of the earth's deep interior, *Geophysical Journal International*, **57**(2), 507–534.

Masters, G. & Gubbins, D., 2003. On the resolution of density within the Earth, *Phys. Earth Planet. Inter.* , **140**(1-3), 159–167.

Masters, G., Laske, G., Bolton, H., & Dziewonski, A., 2000a. The relative behavior of shear velocity, bulk sound speed, and compressional velocity in the mantle: Implications for chemical and thermal structure, *Washington DC American Geophysical Union Geophysical Monograph Series*, **117**, 63–87.

Masters, G., Laske, G., & Gilbert, F., 2000b. Matrix autoregressive analysis of free-oscillation coupling and splitting, *Geophys. J. Int.* , **143**(2), 478–489.

McNamara, A. K., 2019. A review of large low shear velocity provinces and ultra low velocity zones, *Tectonophysics*, **760**, 199–220.

McNamara, A. K. & Zhong, S., 2005. Thermochemical structures beneath Africa and the Pacific Ocean, *Nature*, **437**(7062), 1136–1139.

Menke, W., 1989. Geophysical data analysis: discrete inverse theory, *Geophysical Data Analysis, Aca-*

demic, San Diego, California.

Mooney, W., Laske, G., & Masters, T., 1998. CRUST 5.1: A global crustal model at $5\times 5\ ^{\circ}$, *J. Geophys. Res.* , **103**(B1), 727–747.

Mosca, I., Cobden, L., Deuss, A., Ritsema, J., & Trampert, J., 2012. Seismic and mineralogical structures of the lower mantle from probabilistic tomography, *J. Geophys. Res.* , **117**(B6), B06304.

Moulik, P. & Ekström, G., 2014. An anisotropic shear velocity model of the Earth's mantle using normal modes, body waves, surface waves and long-period waveforms, *Geophys. J. Int.* , **199**(3), 1713–1738.

Moulik, P. & Ekström, G., 2016. The relationships between large-scale variations in shear velocity, density, and compressional velocity in the Earth's mantle, *J. Geophys. Res.* , **121**(4), 2737–2771.

Nolet, G., 2008. A breviary of seismic tomography, *A Breviary of Seismic Tomography, by Guust Nolet, Cambridge, UK: Cambridge University Press, 2008.*

Oganov, A. & Ono, S., 2004. Theoretical and experimental evidence for a post-perovskite phase of MgSiO3 in Earth's D" layer, *Nature* , **430**(6998), 445–448.

Pijpers, F. & Thompson, M., 1992. Faster formulations of the optimally localized averages method for helioseismic inversions, *Astronomy and Astrophysics*, **262**, L33–L36.

Pijpers, F. & Thompson, M., 1994. The sola method for helioseismic inversion, *Astronomy and Astrophysics*, **281**, 231–240.

Rawlinson, N. & Spakman, W., 2016. On the use of sensitivity tests in seismic tomography, *Geophysical Journal International*, **205**(2), 1221–1243.

Rawlinson, N., Fichtner, A., Sambridge, M., & Young, M. K., 2014. Seismic tomography and the assessment of uncertainty, *Advances in geophysics*, **55**, 1–76.

Resovsky, J. S. & Ritzwoller, M. H., 1998. New and refined constraints on three-dimensional Earth structure from normal modes below 3 mHz, *J. Geophys. Res.* , **103**(B1), 783–810.

Restelli, F., Koelemeijer, P., & Ferreira, A., 2023. Normal mode observability of radial anisotropy in the earth's mantle, *Geophysical Journal International*, **233**(1), 663–679.

Ringler, A. T., Anthony, R. E., Davis, P., Ebeling, C., Hafner, K., Mellors, R., Schneider, S., & Wilson, D. C., 2022. Improved resolution across the global seismographic network: A new era in low-frequency seismology, *The Seismic Record*, **2**(2), 78–87.

Ritsema, J. & van Heijst, H.-J., 2002. Constraints on the correlation of P-and S-wave velocity heterogeneity in the mantle from P, PP, PPP and PKPab traveltimes, *Geophys. J. Int.* , **149**(2), 482–489.

Ritsema, J., van Heijst, H.-J., & Woodhouse, J., 1999. Complex shear wave velocity structure imaged beneath Africa and Iceland, *Science* , **286**(5446), 1925.

Ritsema, J., McNamara, A. K., & Bull, A. L., 2007. Tomographic filtering of geodynamic models: Implications for model interpretation and large-scale mantle structure, *J. Geophys. Res.* , **112**(B1).

Ritsema, J., Deuss, A., van Heijst, H.-J., & Woodhouse, J. H., 2011. S40RTS: a degree-40 shear-velocity model for the mantle from new Rayleigh wave dispersion, teleseismic traveltime and normal-mode splitting function measurements, *Geophys. J. Int.* , **184**(3), 1223–1236.

Robson, A., Lau, H. C., Koelemeijer, P., & Romanowicz, B., 2022. An analysis of core–mantle boundary stoneley mode sensitivity and sources of uncertainty, *Geophysical Journal International*, **228**(3), 1962–1974.

Romanowicz, B., 2001. Can we resolve 3D density heterogeneity in the lower mantle?, *Geophys. Res. Lett.* , **28**(6), 1107–1110.

Schneider, S. & Deuss, A., 2021. A new catalogue of toroidal-mode overtone splitting function measurements, *Geophysical Journal International*, **225**(1), 329–341.

Schuberth, B., Bunge, H.-P., & Ritsema, J., 2009. Tomographic filtering of high-resolution mantle circulation models: Can seismic heterogeneity be explained by temperature alone?, *Geophys. Geochem. Geosys.* , **10**(5).

Su, W. & Dziewonski, A., 1997. Simultaneous inversion for 3-D variations in shear and bulk velocity in the mantle, *Phys. Earth Planet. Inter.* , **100**(1-4), 135–156.

Tesoniero, A., Cammarano, F., & Boschi, L., 2016. S- to- P heterogeneity ratio in the lower mantle and thermo-chemical implications, *Geophys. Geochem. Geosys.* , **17**(7), 2522–2538.

Trampert, J., 1998. Global seismic tomography: the inverse problem and beyond, *Inverse Problems*, **14**(3), 371.

Trampert, J. & Snieder, R., 1996. Model estimations biased by truncated expansions: possible artifacts in seismic tomography, *Science*, **271**(5253), 1257–1260.

Trampert, J., Deschamps, F., Resovsky, J., & Yuen, D., 2004. Probabilistic tomography maps chemical heterogeneities throughout the lower mantle, *Science* , **306**(5697), 853.

Wessel, P., Smith, W. H. F., Scharroo, R., Luis, J., & Wobbe, F., 2013. Generic mapping tools: Improved version released, *Eos, Transactions American Geophysical Union*, **94**(45), 409–410.

Woodhouse, J., Giardini, D., & Li, X., 1986. Evidence for inner core anisotropy from free oscillations, *Geophys. Res. Lett.* , **13**(13), 1549–1552.

Zaroli, C., 2016. Global seismic tomography using backus–gilbert inversion, *Geophysical Journal International*, **207**(2), 876–888.

Zaroli, C., 2019. Seismic tomography using parameter-free backus–gilbert inversion, *Geophysical Journal International*, **218**(1), 619–630.

Zaroli, C., Koelemeijer, P., & Lambotte, S., 2017. Toward seeing the earth's interior through unbiased tomographic lenses, *Geophysical Research Letters*, **44**(22), 11–399.

FIGURES

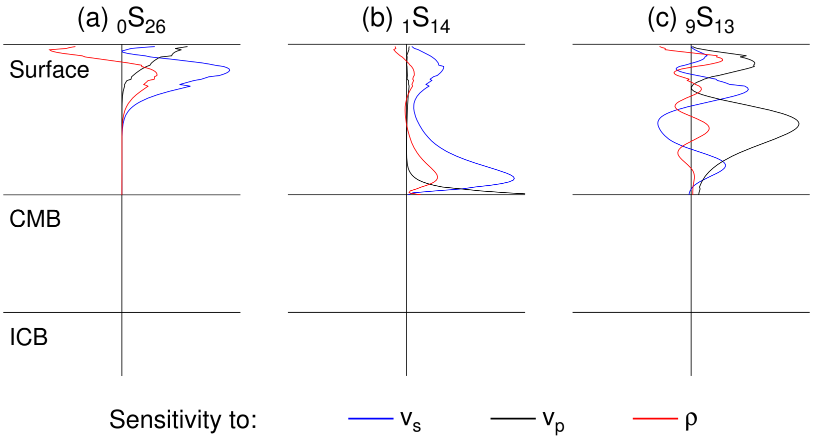

Figure 1. Examples of spheroidal mode sensitivity kernels for mantle structure at degree $s = 2$. We show the sensitivity to shear-wave velocity v_s (blue), compressional-wave velocity v_p (black) and density ρ (red), calculated for the anisotropic PREM model (Dziewonski & Anderson 1981). Horizontal lines indicate the surface and the radii of the core-mantle boundary (CMB) and inner core boundary (ICB). Each panel is normalised independently. Kernels for other spherical harmonic degrees are presented in Supplementary Fig. S1. The resolving kernels obtained using SOLA are effectively linear combinations of different normal mode sensitivity kernels.

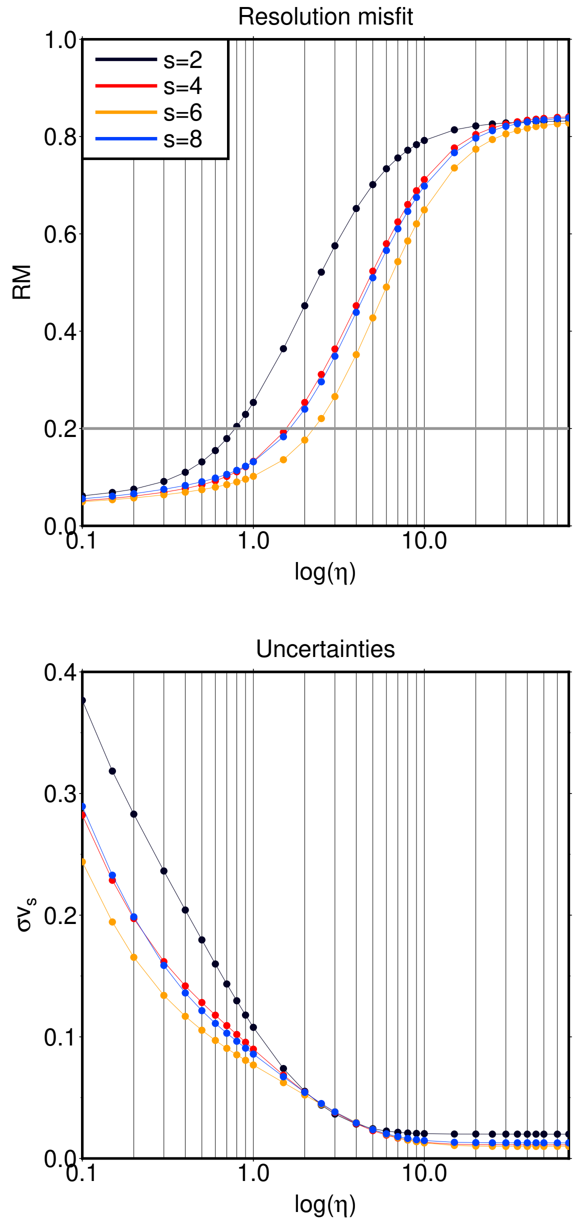

Figure 2. Example trade-off curves of resolution misfit (a) and model uncertainties (b) as a function of trade-off parameter η. Each dot corresponds to a synthetic inversion for v_s including 3D noise (3D-N case, see Section 4.2), here computed for harmonic degrees $s = 2$, 4, 6 and 8 with order $t = 1$. To build complete models of all spherical harmonics, we combine results for different spherical harmonic degrees with the same resolution misfit RM. For example, if we choose a value of 0.2 for RM (grey line, top panel), we would use values of η between ~0.8 (for $s = 2$) and ~2.5 (for $s = 6$).

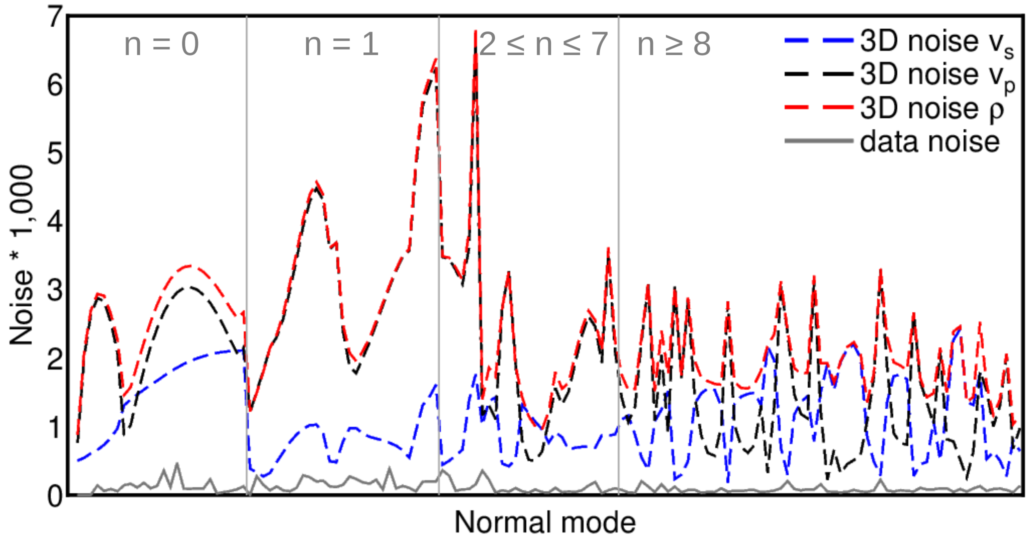

Figure 3. Illustration of typical 3D noise levels, showing noise levels for coefficient c_{20} for v_s (blue), v_p (black) and density (red) for all modes of our data set (horizontal axis). The data uncertainties are also plotted for comparison (grey). Grey vertical lines divide mode branches with different n. While individual mode noise levels are difficult to determine, it is clear that the 3D noise for v_s is lower than that for v_p and density. This is mostly due to the smaller amplitudes of v_p and ρ perturbations in existing mantle models compared to v_s, as well as the sensitivity kernels. Note that the 3D noise levels are significantly larger than the data noise.

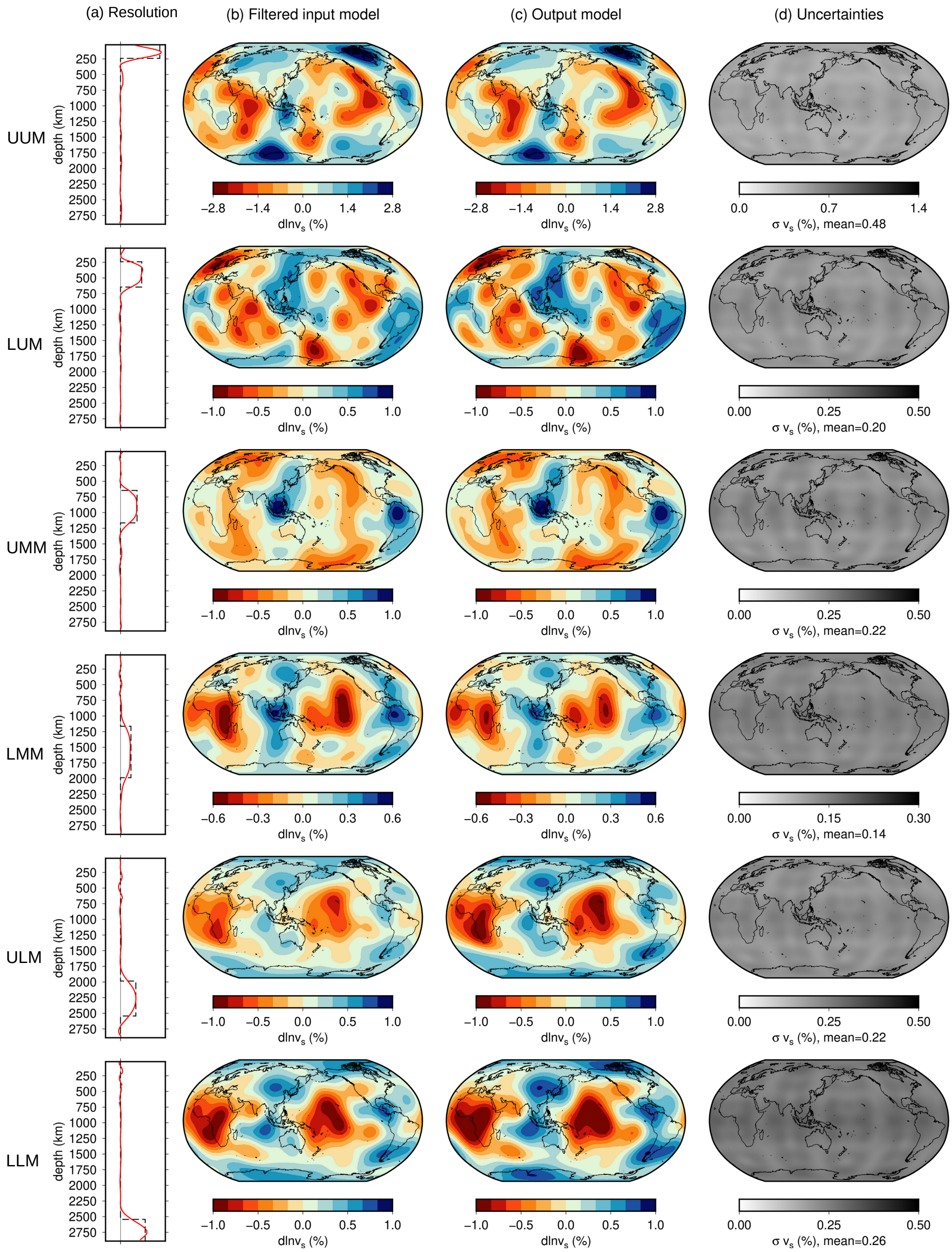

Figure 4. Synthetic inversion results for v_s perturbations with 3D noise (case 3D-N). For each layer (shown in different rows) we present: (a) the target and resolving kernels (black and red lines, respectively); (b) the input model S20RTS filtered through the relevant resolving kernel; (c) the output model estimate; (d) the output model uncertainties. In (a), we only show the resolving kernel for spherical harmonic coefficient c_{20}, as other resolving kernels have the same shape as set by our inversion procedure (Section 4.2). The uncertainties are generally very uniform due to the even data coverage provided by normal modes.

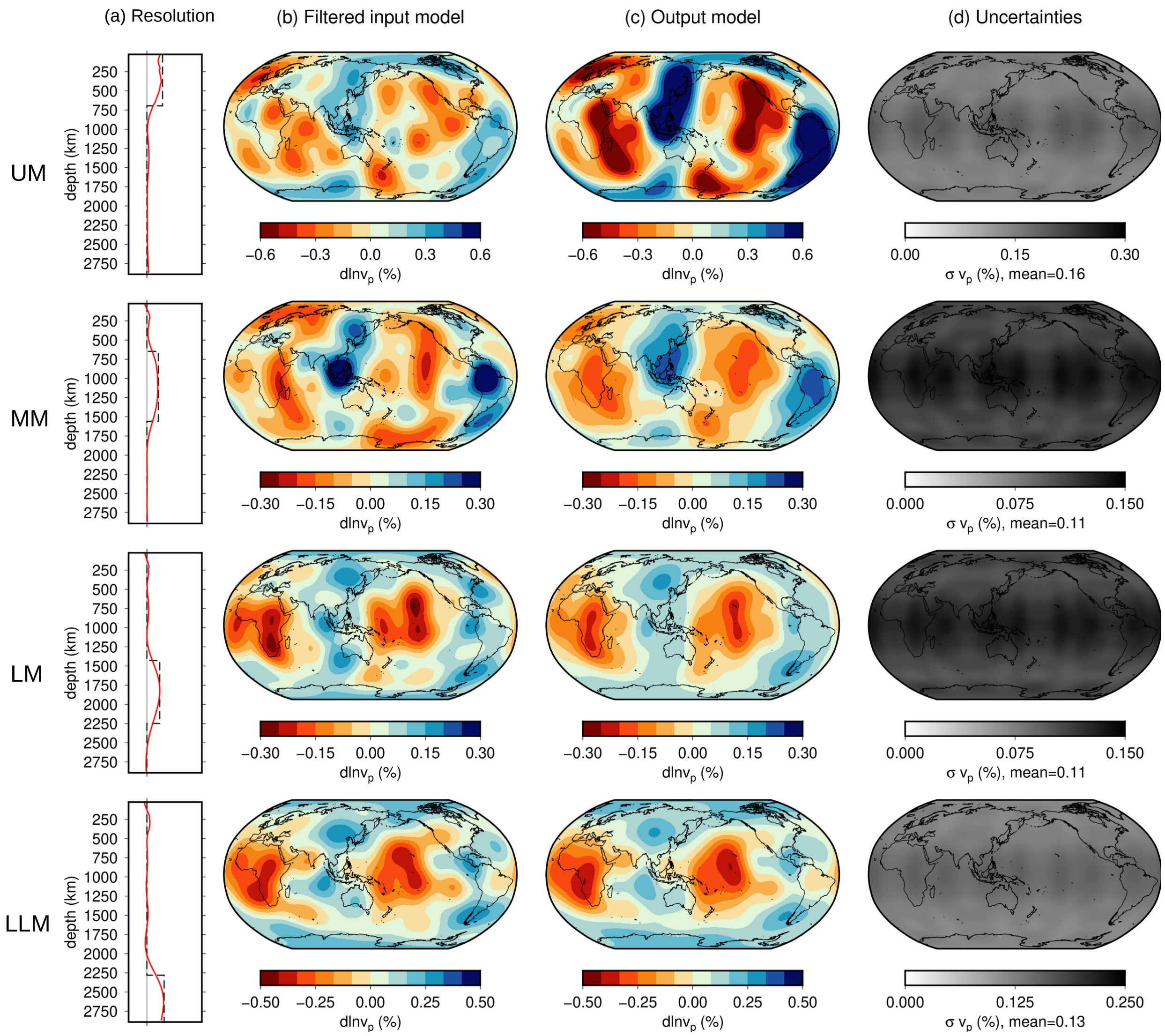

Figure 5. Synthetic inversion results for v_p perturbations with 3D noise (case 3D-N). All panels and details are similar as in Fig. 4

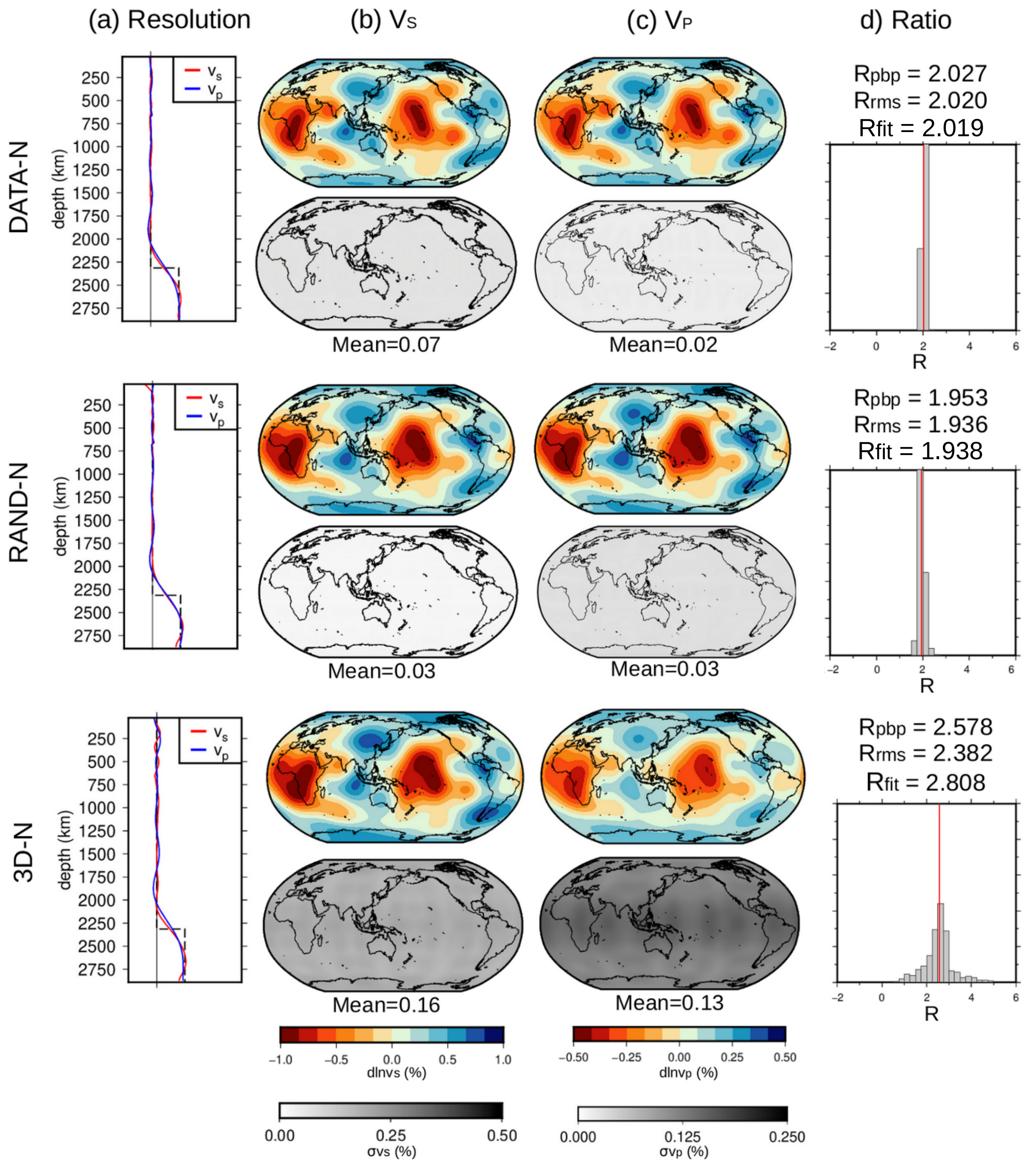

Figure 6. Synthetic inversion results for the ratio $R = \mathrm{dln}v_s/\mathrm{dln}v_p$. We show results for the three different noise cases (DATA-N, RAND-N and 3D-N). For each case, we show: (a) the $\mathrm{dln}v_s$ (red) and $\mathrm{dln}v_p$ (blue) resolving kernels and target kernel (black); (b) the $\mathrm{dln}v_s$ model estimate and associated uncertainties; (c) the $\mathrm{dln}v_p$ model estimate and associated uncertainties; (d) histograms resulting from a point-by-point division between the two maps ($\mathrm{dln}v_s/\mathrm{dln}v_p$), with the vertical red line indicating the mean of the distribution (R_{pbp}). We also indicate the value of the ratio R calculated using the RMS and regression-fit approaches (see text). The maximum of the scale for the v_s maps is twice that for the v_p maps, so that when the two maps have similar patterns and colour intensity we can directly – and qualitatively – infer that the ratio is close to 2.

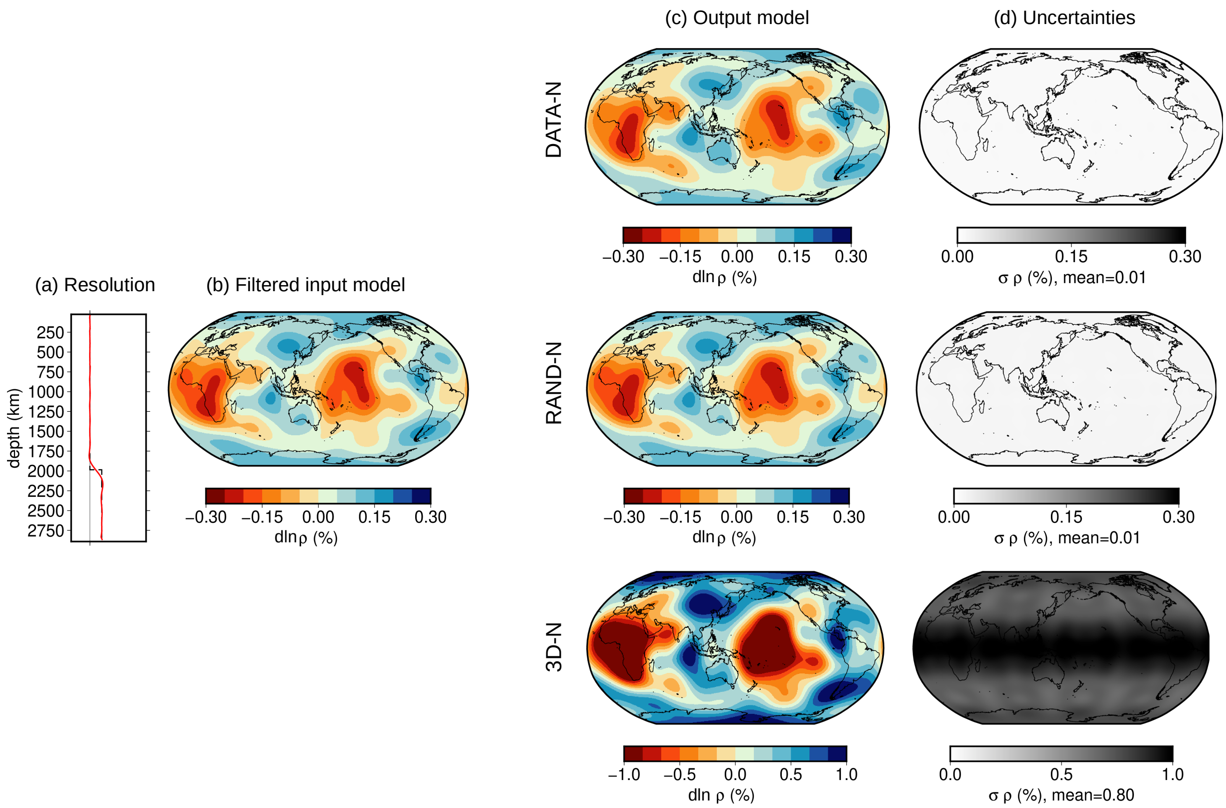

Figure 7. Synthetic inversion results for density perturbations with only data noise (DATA-N), random noise (RAND-N) and also 3D noise (3D-N). We only show results for a layer on top of the core-mantle boundary, showing (a) the target and resolving kernels (black and red lines, respectively); (b) the input model S20RTS filtered through the relevant resolving kernel; (c) the output model estimates for the three different cases; (d) the output model uncertainties.

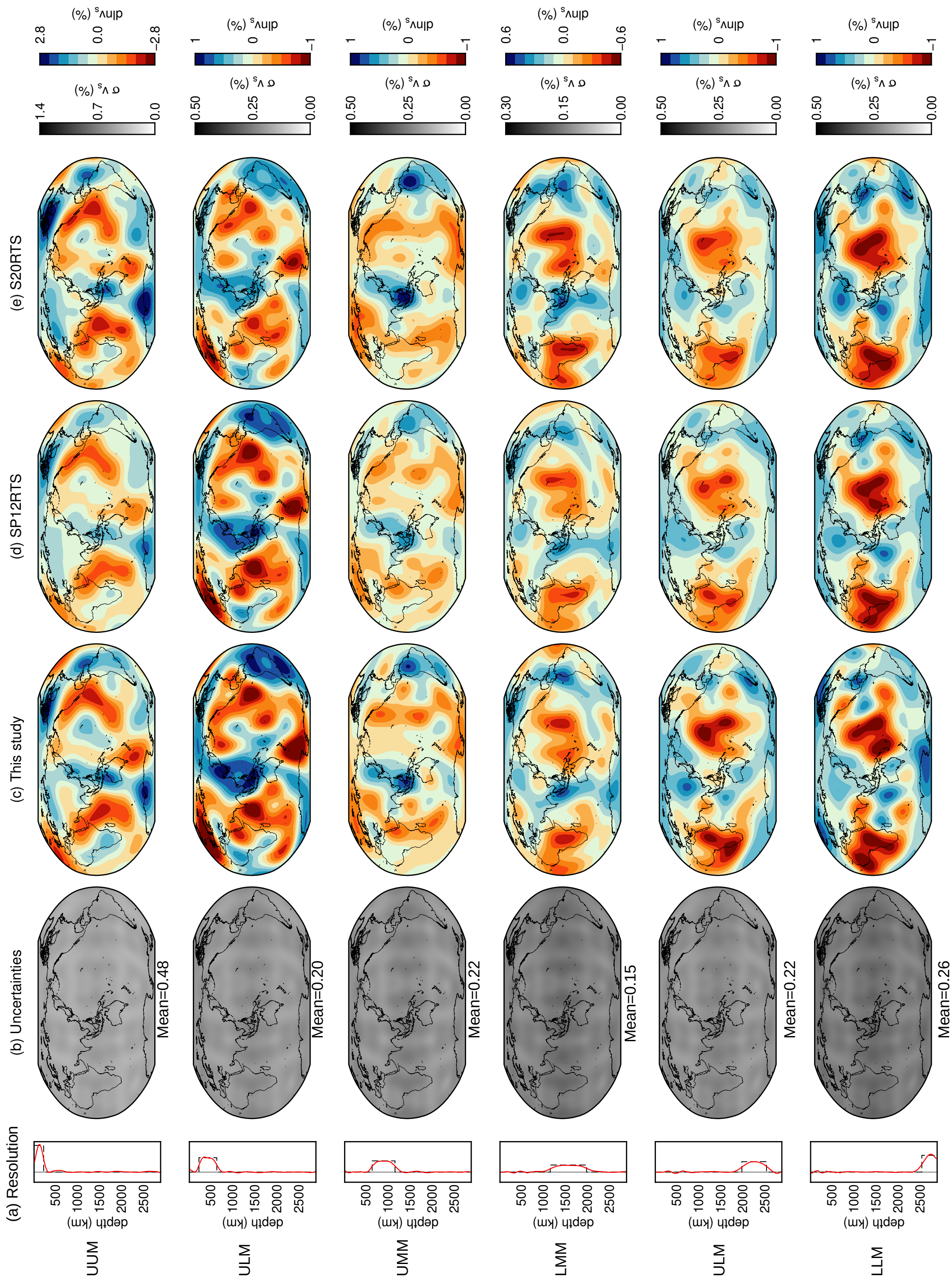

Figure 8. Real data inversion results for v_s perturbations. For each layer (given as different rows) we show: (a) the target and resolving kernels (black and red lines, respectively); (b) the model uncertainties; (c) the model estimate of v_s perturbations; (d) the shear-wave velocity structure of model SP12RTS; (e) the shear-wave velocity structure of model S20RTS. The mean layer absolute uncertainty is indicated at the bottom of each uncertainty map. The uncertainty and resolution information that accompany our model are not provided by the SP12RTS and S20RTS models.

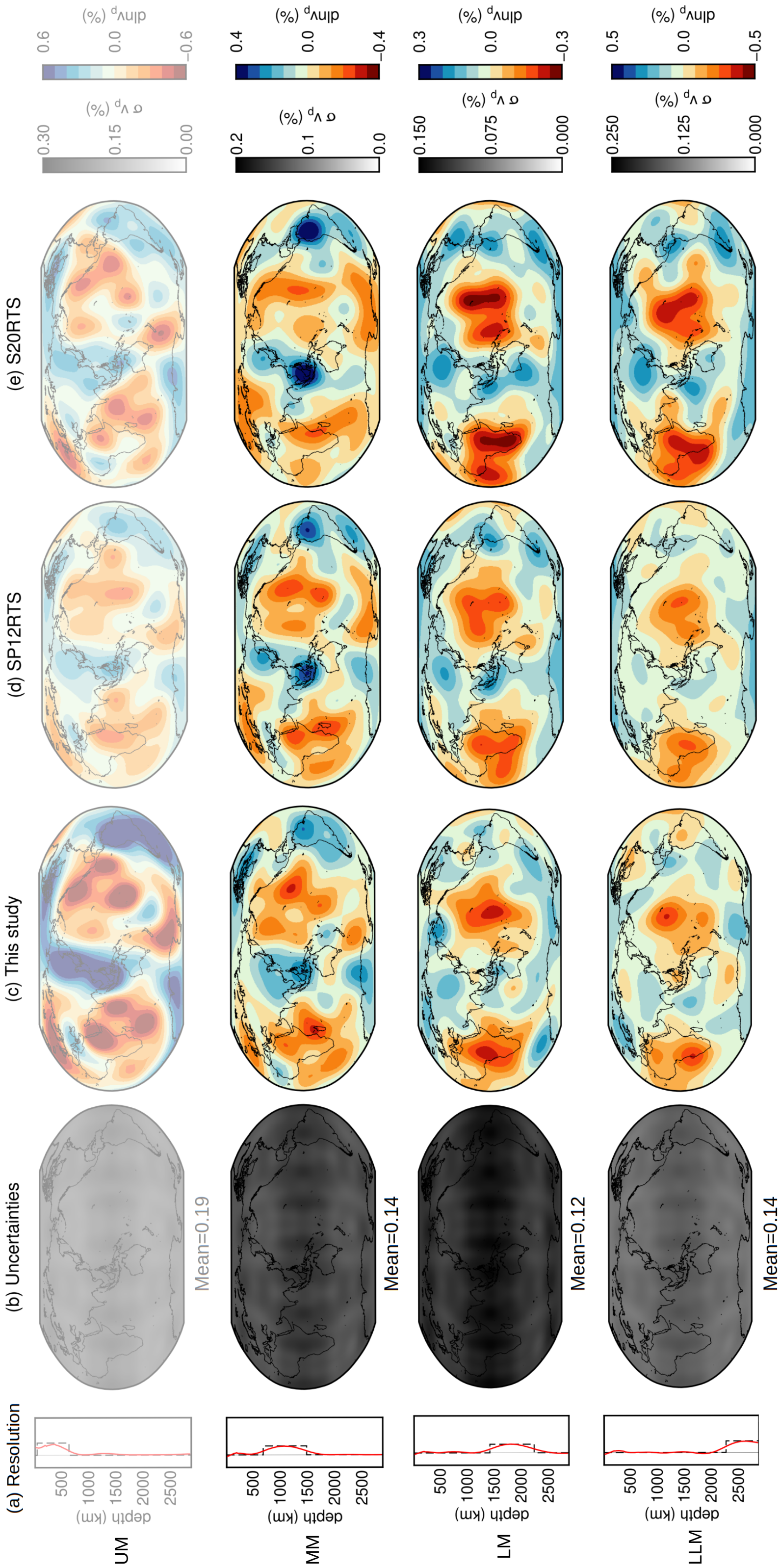

Figure 9. Real data inversion results for v_p perturbations. All panels and details are similar as in Fig. 8, except that the v_p perturbations in S20RTS are obtained by scaling the v_s perturbations, while they are independently inverted for in SP12RTS. The mean layer absolute uncertainty is indicated at the bottom of each uncertainty map. Note that the structure in the UM layer should not be interpreted based on the synthetic test results of Fig. 5.

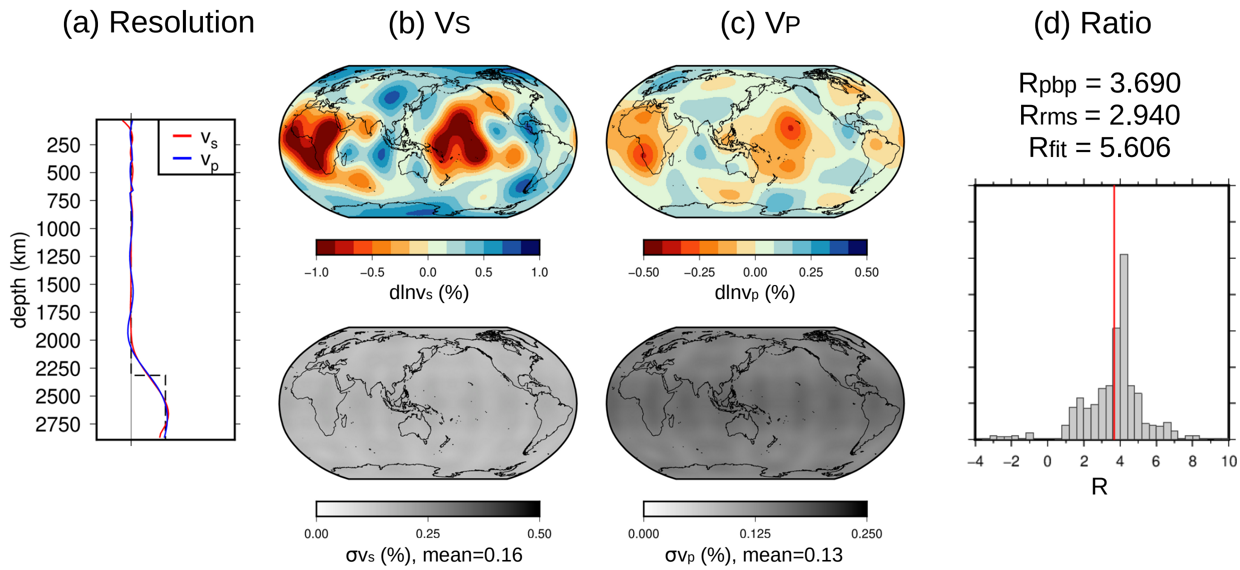

Figure 10. Real data inversion results for the ratio $R = \mathrm{dln}v_s/\mathrm{dln}v_p$. As in Fig. 6, we show: (a) the $\mathrm{dln}v_s$ (red) and $\mathrm{dln}v_p$ (blue) resolving kernels and target kernel (black); (b) the $\mathrm{dln}v_s$ model estimate and uncertainties; (c) the $\mathrm{dln}v_p$ model estimate and uncertainties; (d) the histogram resulting from a point-by-point division between the two maps ($\mathrm{dln}v_s/\mathrm{dln}v_p$), with the vertical red line indicating the mean of the distribution (R_{pbp}). We also indicate the value of the ratio R calculated as the mean of the ratio between the RMS values of $\mathrm{dln}v_s$ and $\mathrm{dln}v_p$ (R_{rms}) and as the slope of the best-fitting line between $\mathrm{dln}v_s$ and $\mathrm{dln}v_p$ perturbations (R_{fit}).

Supplementary material for "Robust estimates of the ratio between S- and P-wave velocity anomalies in the Earth's mantle using normal modes"

Federica Restelli[1,†], Christophe Zaroli[2] & Paula Koelemeijer[1,3*]

[1] Department of Earth Sciences, Queen's Building. Royal Holloway University of London, Egham Hill, Egham, Surrey, TW20 0EX, United Kingdom
[2] Institut Terre et Environnement de Strasbourg, UMR 7063, Université de Strasbourg, EOST/CNRS, 67084 Strasbourg cedex, France.
[3] Department of Earth Sciences, University of Oxford, South Parks Road, Oxford, OX1 3AN UK, United Kingdom
† Corresponding author. Email: federica.restelli.2019@live.rhul.ac.uk
* Email: paula.koelemeijer@earth.ox.ac.uk

Contents:

- Supplementary Text
- Supplementary Table S1
- Supplementary Figures S1-S8.

Table S1 lists the 16 tomographic models used in the calculation of the 3D noise (as detailed in Section 3.4 in the main text). In some studies, v_p perturbations were directly inverted for, in other studies they were scaled from v_s perturbations (using particular $\mathrm{dln}v_p/\mathrm{dln}v_s$ scaling factors as indicated in the table). Density perturbations are always obtained by scaling them from v_s perturbations, with the $\mathrm{dln}\rho/\mathrm{dln}v_s$ scaling factor also given in the table.

Table S1: List of tomography models (in chronological order) used for the estimation of the 3D noise, including any scaling factors for v_p and density perturbations. We scale v_p and ρ according to the original studies, wherever this information is provided (bold values). If no information on the scaling was provided, we set $\mathrm{dln}v_p/\mathrm{dln}v_s$=0.5 and $\mathrm{dln}\rho/\mathrm{dln}v_s$=0.3.

Model	$\mathrm{dln}v_p/\mathrm{dln}v_s$	$\mathrm{dln}\rho/\mathrm{dln}v_s$	Ref.
S20RTS	**0.5**	0.3	Ritsema et al. (1999)
TX2011	0.5	0.3	Grand (2002)
PRI-05	Inverted for	0.3	Montelli et al. (2006)
HMSL-06	Inverted for	0.3	Houser et al. (2008)
GyPSuM	Inverted for	0.3	Simmons et al. (2010)
SAW642ANb	**0.5**	**0.33**	Panning et al. (2010)
SEMum	**0.5**	**0.3**	Lekić and Romanowicz (2011)
S40RTS	**0.5** (0 km) - **0.33** (2891 km)	**0.5**	Ritsema et al. (2011)
savani	0.5	0.3	Auer et al. (2014)
SEMUCB-WM1	**0.5**	0.3	French and Romanowicz (2014)
S362WMANI+M	**0.55**	0.3	Moulik and Ekström (2014)
SGLOBE-rani	**0.5**	**0.4**	Chang et al. (2014)
SPani	Inverted for	0.3	Tesoniero et al. (2015)
SP12RTS	Inverted for	**0.3**	Koelemeijer et al. (2016)
s10mean	0.5	0.3	Doubrovine et al. (2016)
TX2015	0.5	0.3	Lu and Grand (2016)

Fig. S1 shows isotropic sensitivity kernels for degrees $s = 2, 4, 6, 8$ for the same spheroidal modes as in Figure 1 in the main text. Although the sensitivity to v_s and ρ depends on the spherical harmonic degree, Fig. S1 indicates that kernels for different degrees are not significantly different. Kernels for v_p do not depend on the spherical harmonic degree and are therefore not shown.

In Fig. S2 we show the results for both the upper (top) and lower mantle (bottom) from synthetic tests where we vary how the crust is treated. In the rows titled "CORRECTION", we correct the splitting functions using the crustal thickness from model CRUST5.1 (in addition to surface topography and water level) before performing SOLA inversions. In the rows titled "NOISE", the crustal thickness is not included in the crustal corrections, but instead part of the 3D noise. To do this, we compute the 3D noise arising from crustal thickness uncertainties in a similar way as explained in Section 3.5: we calculate splitting function predictions for just the crustal thickness model (no mantle structure), using either model CRUST5.1 (Mooney et al., 1998), model CRUST2.0 (Laske et al., 2013), or the crustal thickness models developed with SGLOBE-rani (Chang et al., 2015) and SEMUCB-WM1 (French and Romanowicz, 2014). The 3D noise of each mode and each coefficient is approximated by the largest predicted value, which is a conservative estimate. The output maps obtained in both cases look very similar to each other, with differences in amplitudes less than 5%. This justifies our choice to use crustal thickness corrections instead of including it in the noise.

Fig. S3 and S4 show the v_s perturbations obtained from the application of SOLA to the cases DATA-N and RAND-N, respectively. As expected, the uncertainties are significantly lower than we add additional 3D noise (Fig. 4 in the main text), with the relative uncertainty being between 4.7 and 15.5% for DATA-N and between 3.8 and 14.8% for RAND-N. Apart from the reduction in the uncertainties, the use of only data or random noise does not lead to significant differences compared to the map obtained with 3D noise (case 3D-N).

Fig. S5 and S6 show the v_p perturbations obtained from the application of SOLA to the cases DATA-N and RAND-N, respectively. In both cases, the relative uncertainties are always below 13% and the output maps closely resemble the input model both in terms of pattern and amplitudes. When 3D noise is added, this changes significantly and we are not able to recover the pattern and/or the amplitudes of v_p in the first three layers. Moreover, in those layers the relative uncertainties surpass our threshold of 50%. This suggest that the 3D noise (especially from v_s) affects both the model uncertainties and the recovered v_p structure strongly.

Fig. S7 presents our values of R in the four layers that span the whole mantle, estimated by taking the mean of the histograms or from the slope of the best-fitting line. The ratio increases from the surface to the CMB, in agreement with previous studies, although we would not interpret the results in the upper mantle (UM) layer as $\mathrm{dln}v_p$ amplitudes are biased here (see Section 4.4 in the main text).

Similarly to Fig. S3, Fig. S8 shows results for v_s perturbations in a synthetic test setup, now using the original data uncertainties rather than doubled uncertainties. A comparison between the two figures indicates that, while in both cases we obtain satisfying resolving kernels, the model estimates in Fig. S8 do not resemble the input model at all. This indicates that it is crucial to increase the data uncertainties to ensure stable inversions.

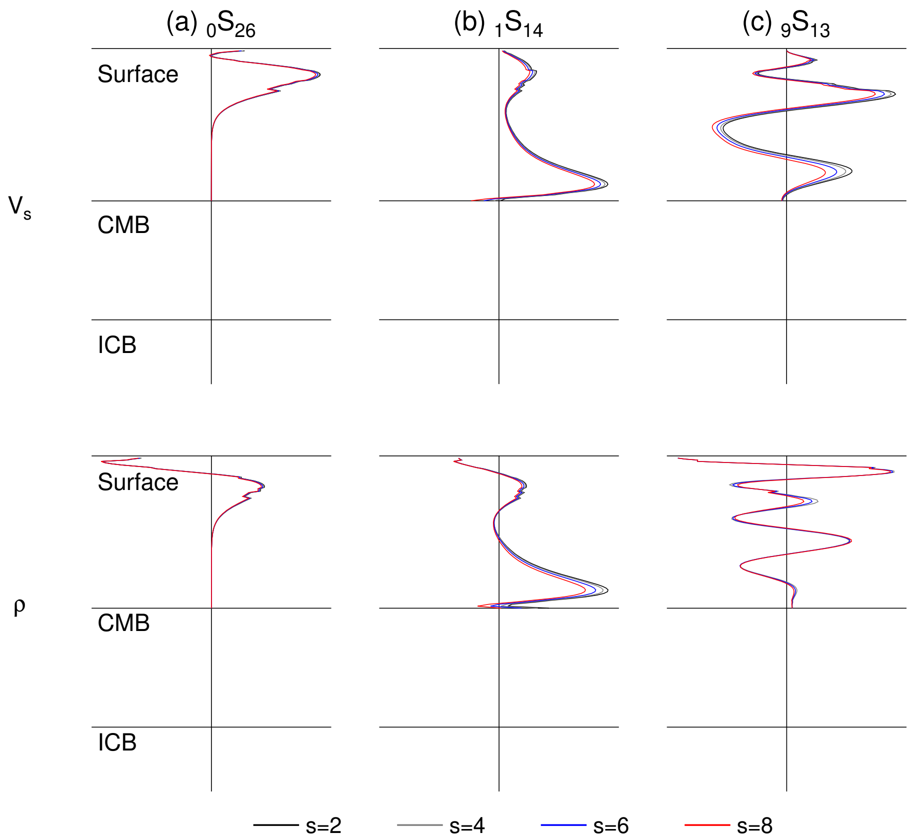

Figure S1: Example sensitivity kernels of spheroidal modes for mantle structure at degrees $s = 2, 4, 6, 8$. We show the sensitivity to shear-wave velocity (top) and density (bottom), calculated for the anisotropic PREM model. Similar to Fig. 1 in the main text.

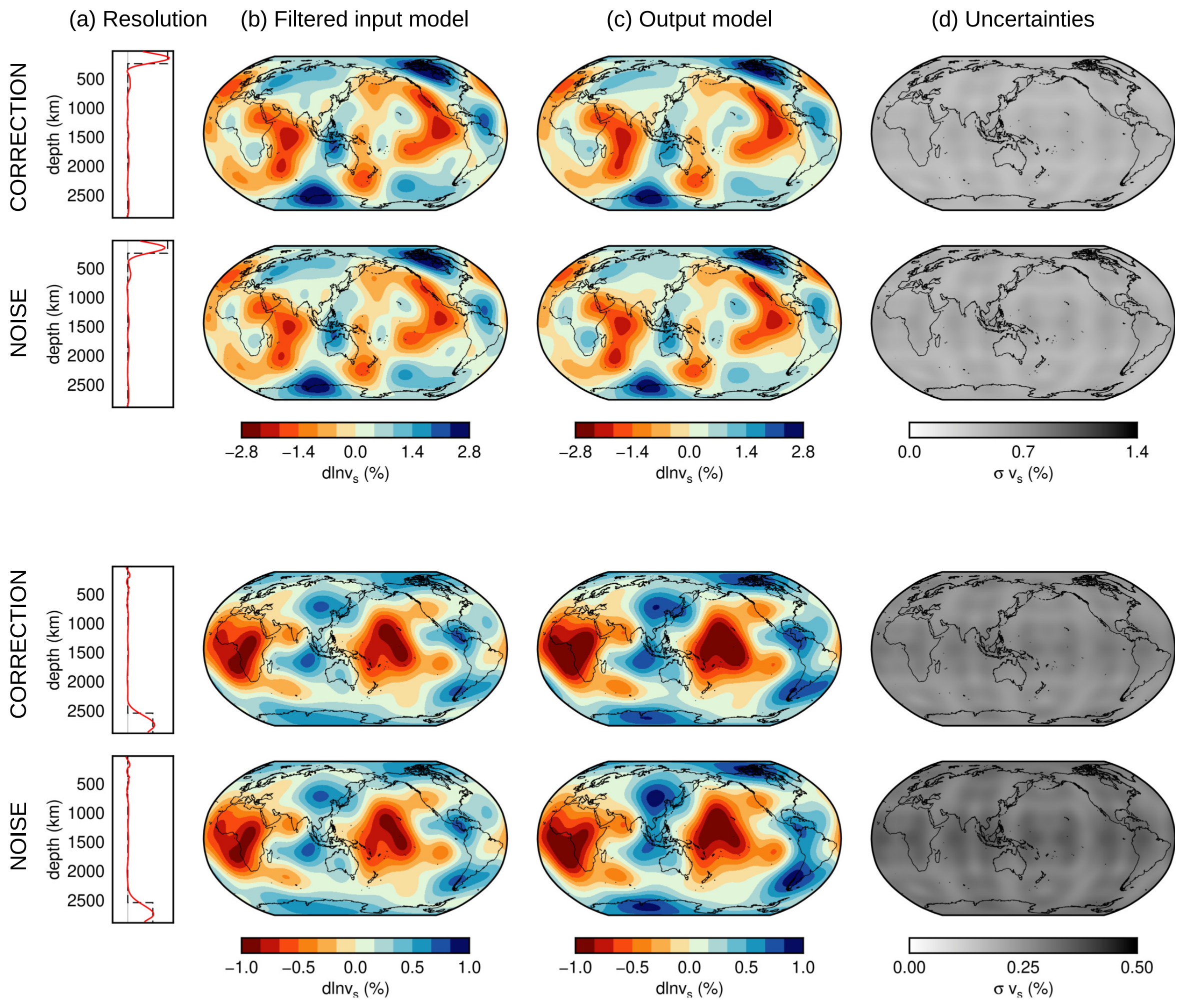

Figure S2: Influence of crustal structure on the synthetic inversion results for v_s perturbations for case 3D-N. For layers in the upper mantle (top) and in the lowermost mantle (bottom), we show: (a) the target and resolving kernels (black and red lines, respectively); (b) the filtered input model; (c) the output model estimate; (d) the output model uncertainties. The crust is either accounted for by crustal corrections (CORRECTION) or included in the 3D noise (NOISE).

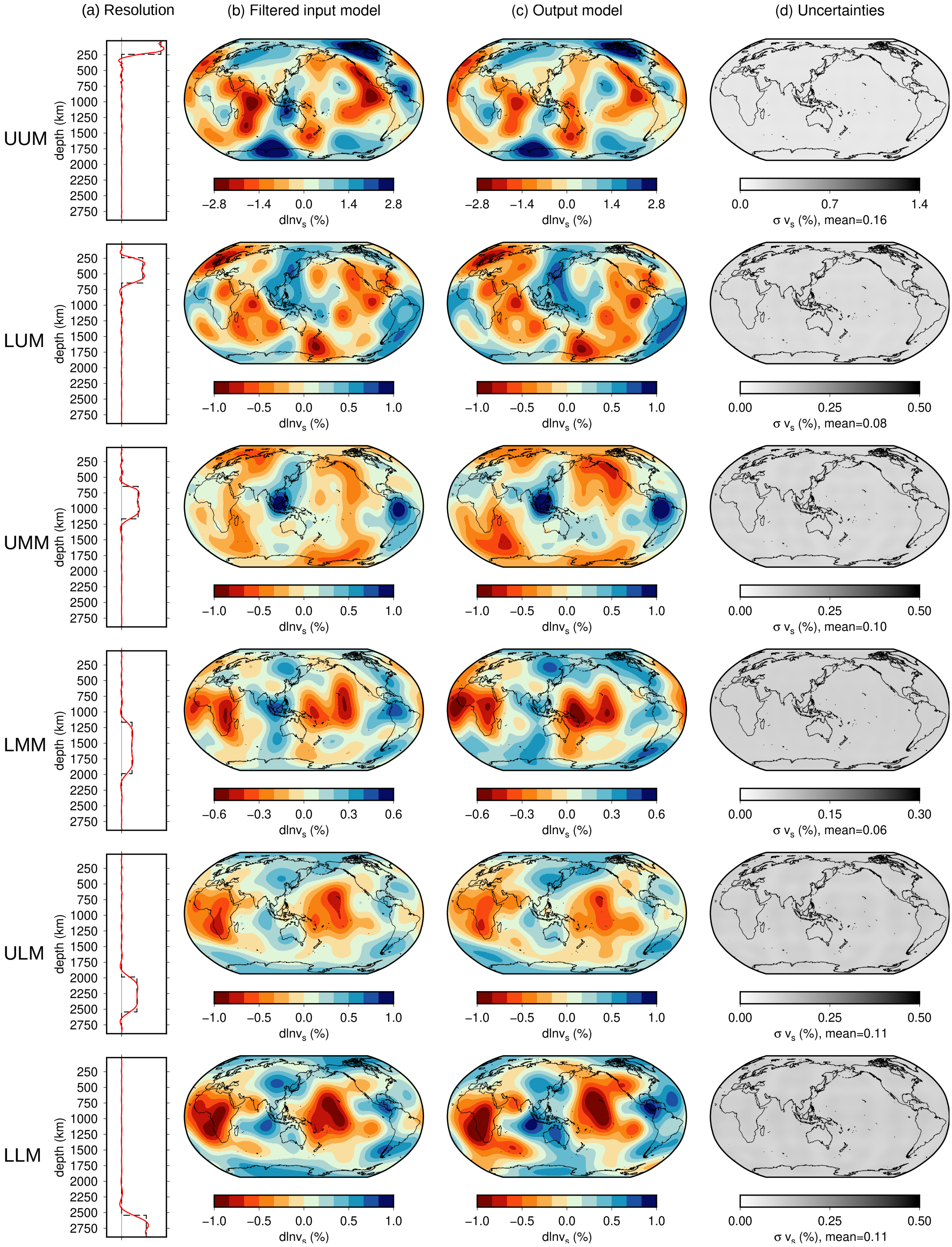

Figure S3: Synthetic inversion results for v_s perturbations with doubled data noise (case DATA-N). Similar to Fig. 4 in the main text.

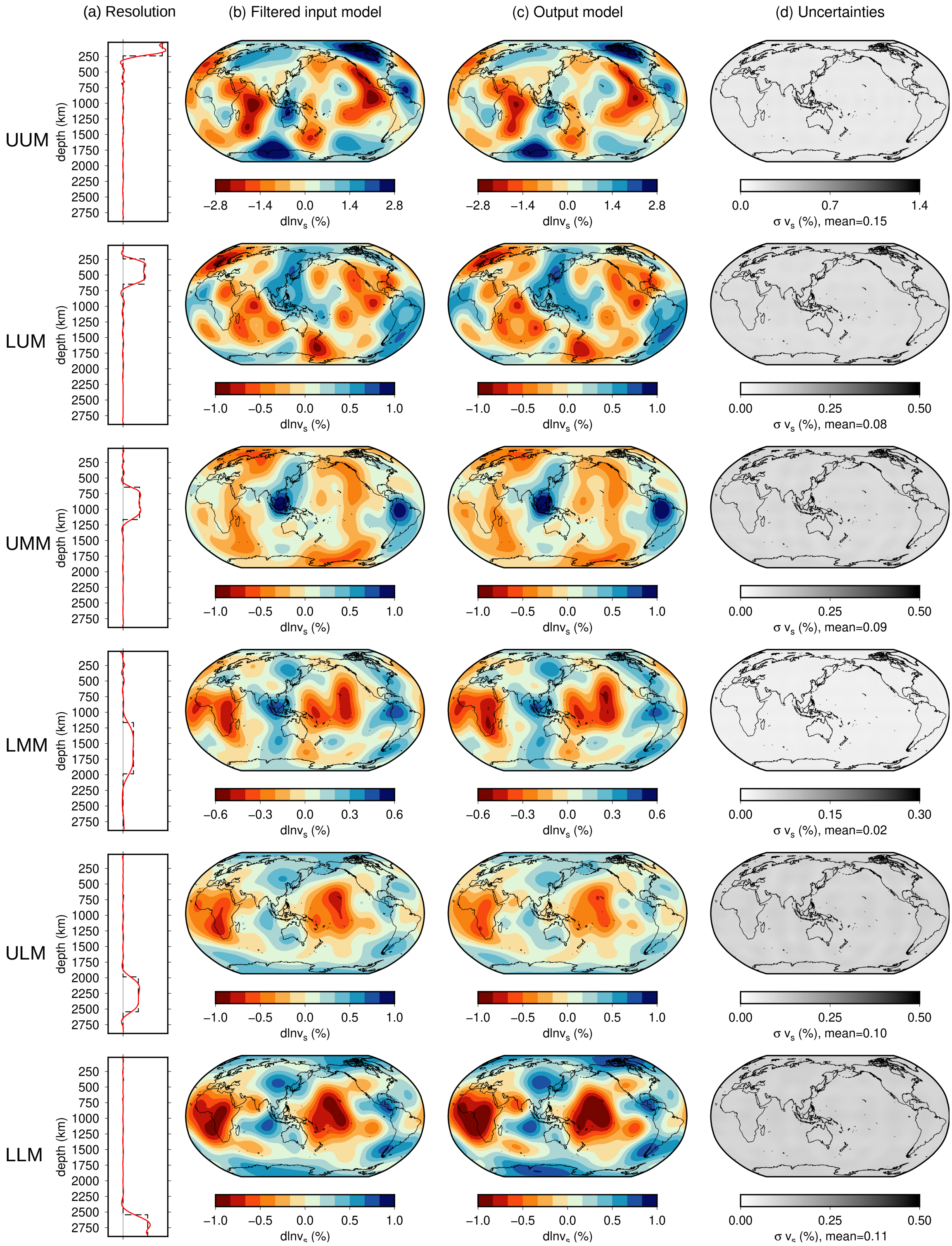

Figure S4: Synthetic inversion results for v_s perturbations with random noise (case RAND-N). Similar to Fig. 4 in the main text.

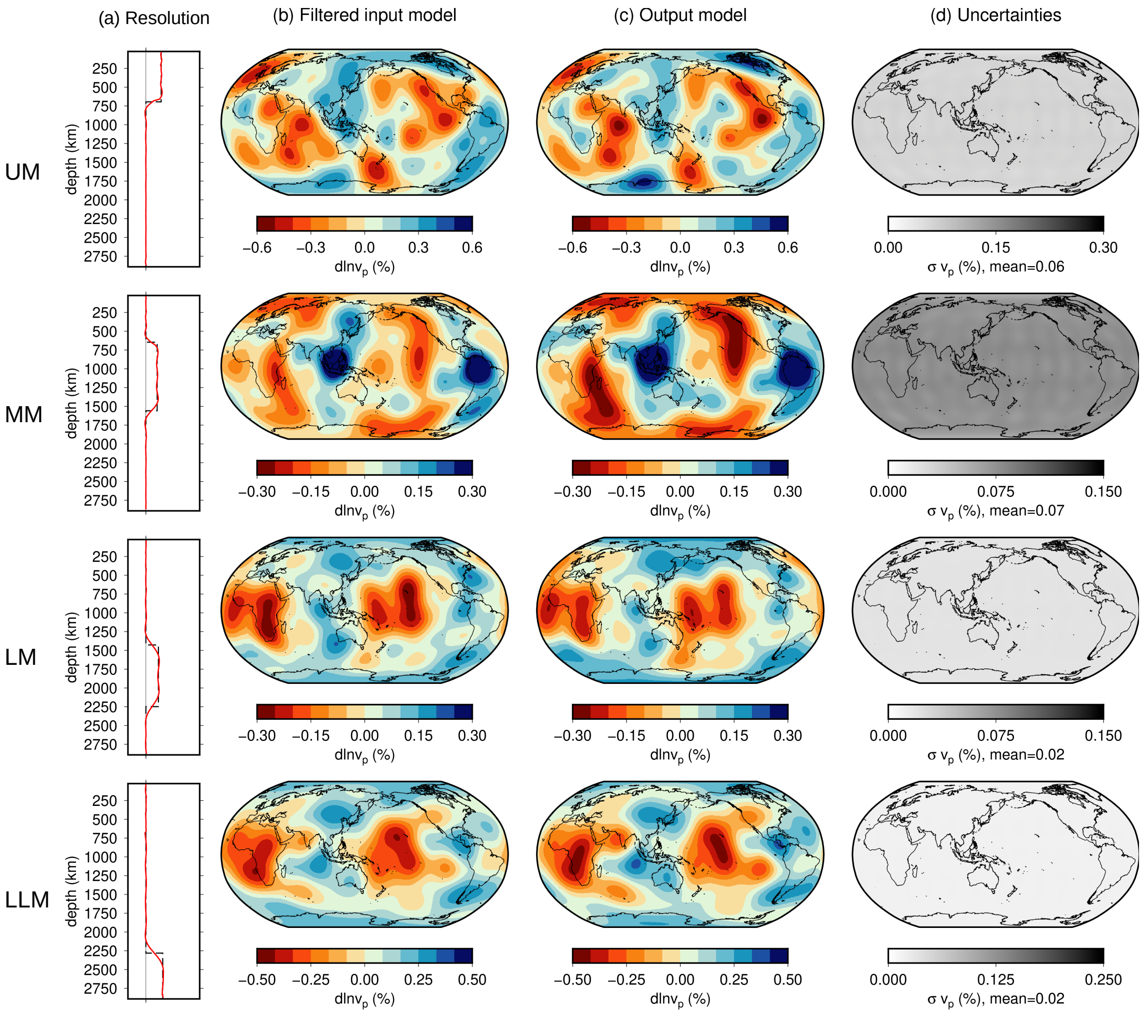

Figure S5: Synthetic inversion results for v_p perturbations with doubled data noise (case DATA-N). Similar to Fig. 5 in the main text.

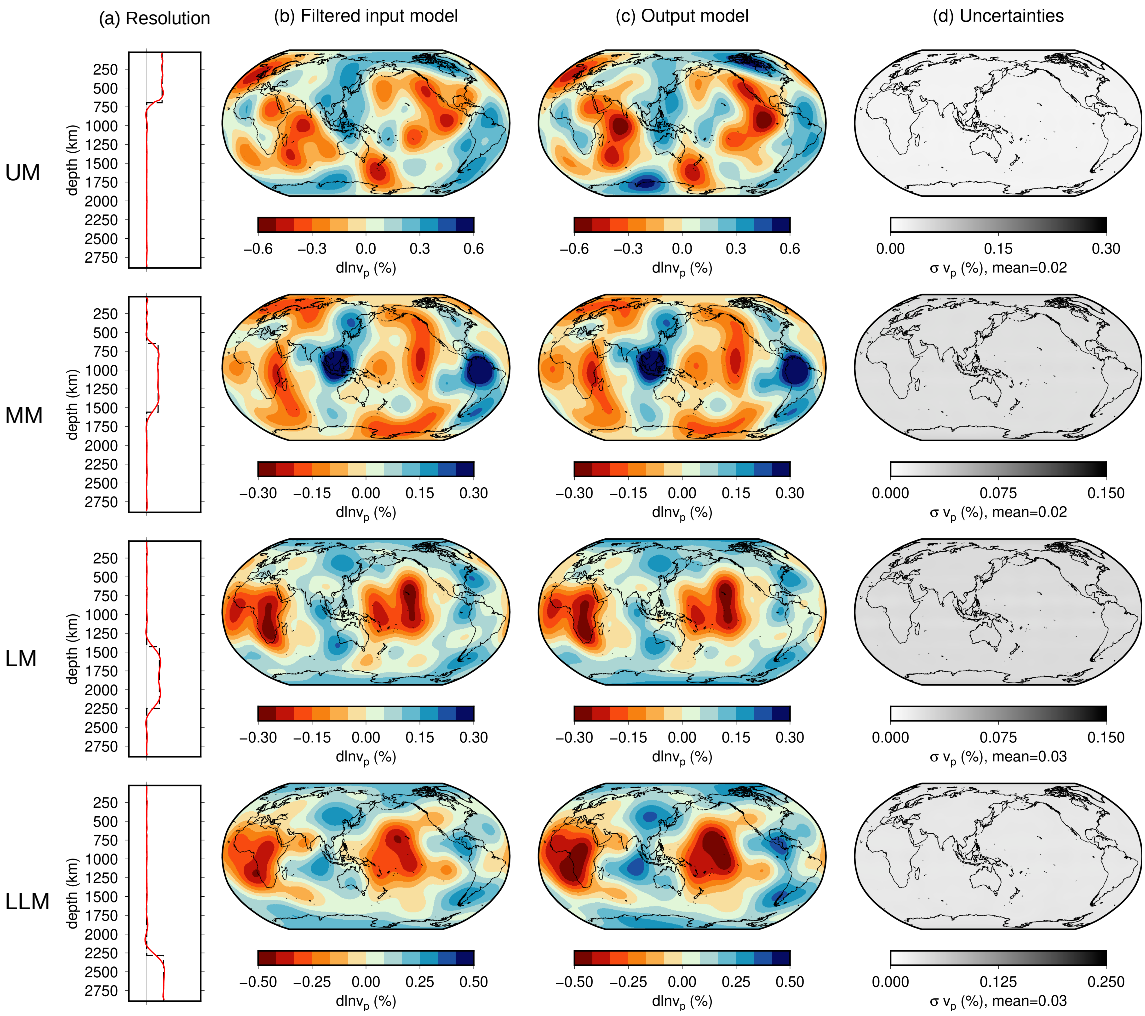

Figure S6: Synthetic inversion results for v_p perturbations with random noise (case RAND-N). Similar to Fig. 5 in the main text.

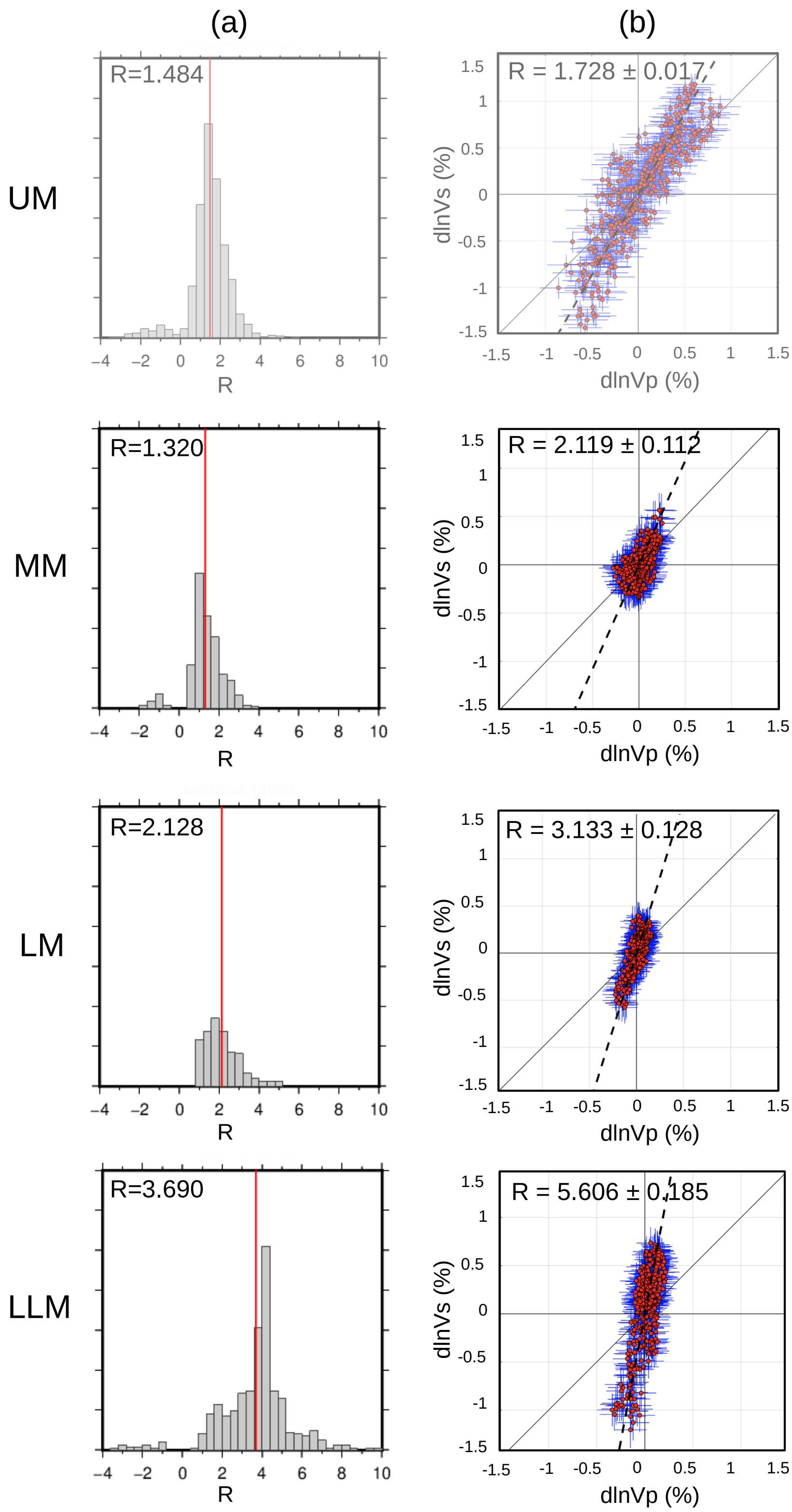

Figure S7: Estimates of the ratio $R = \mathrm{dln}v_s/\mathrm{dln}v_p$ for real data inversions for each of the four layers associated with the resolving kernels in e.g. Fig. 9 in the main text. Here, we illustrate the computation of R as the mean of the histograms resulting from a point-by-point division (a) and as the slope of the best-fitting straight line (b). In panels (b) red circles represent pairs of ($\mathrm{dln}v_p$, $\mathrm{dln}v_s$) for points uniformly located on a sphere, blue lines represent the error bars on both axes. Note that the ratio in the first (upper mantle, UM) layer should not be interpreted given the synthetic test results in Fig. 5 of the main text.

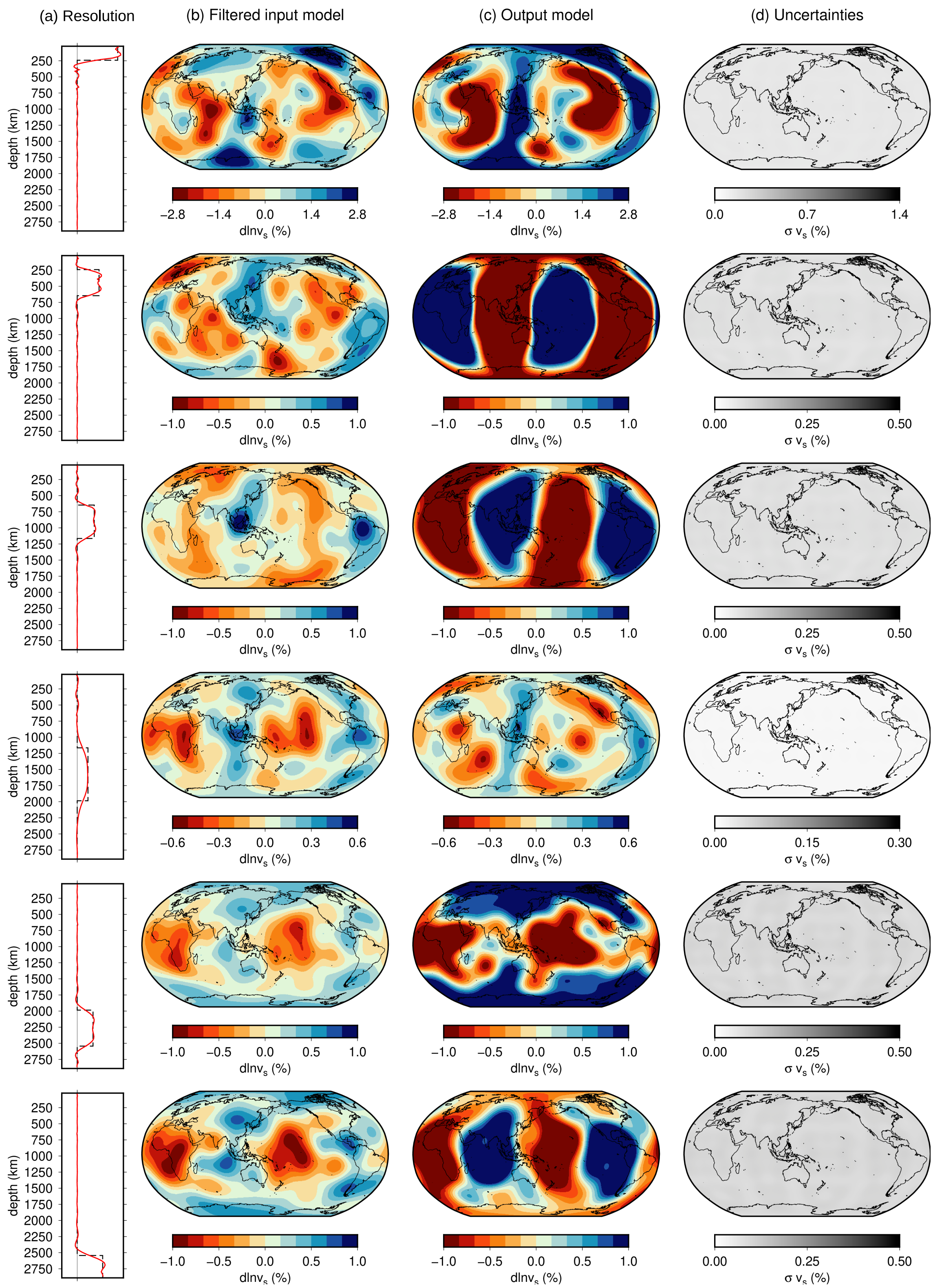

Figure S8: Synthetic inversion results for v_s perturbations, similar to case DATA-N in Fig. S3, but using the original published data uncertainties rather than doubled uncertainties.

Bibliography

Auer, L., Boschi, L., Becker, T., Nissen-Meyer, T., and Giardini, D. (2014). Savani: A variable resolution whole-mantle model of anisotropic shear velocity variations based on multiple data sets. *J. Geophys. Res.* , 119(4):3006–3034.

Chang, S.-J., Ferreira, A. M., Ritsema, J., Heijst, H. J., and Woodhouse, J. H. (2015). Joint inversion for global isotropic and radially anisotropic mantle structure including crustal thickness perturbations. *Journal of Geophysical Research: Solid Earth*.

Chang, S.-J., Ferreira, A. M., Ritsema, J., van Heijst, H. J., and Woodhouse, J. H. (2014). Global radially anisotropic mantle structure from multiple datasets: a review, current challenges, and outlook. *Tectonophysics*, 617:1–19.

Doubrovine, P. V., Steinberger, B., and Torsvik, T. H. (2016). A failure to reject: Testing the correlation between large igneous provinces and deep mantle structures with edf statistics. *Geochemistry, Geophysics, Geosystems*, 17(3):1130–1163.

French, S. and Romanowicz, B. (2014). Whole-mantle radially anisotropic shear velocity structure from spectral-element waveform tomography. *Geophys. J. Int.* , 199(3):1303–1327.

Grand, S. P. (2002). Mantle shear–wave tomography and the fate of subducted slabs. *Philosophical Transactions of the Royal Society of London. Series A: Mathematical, Physical and Engineering Sciences*, 360(1800):2475–2491.

Houser, C., Masters, G., Shearer, P., and Laske, G. (2008). Shear and compressional velocity models of the mantle from cluster analysis of long-period waveforms. *Geophys. J. Int.* , 174(1):195–212.

Koelemeijer, P., Ritsema, J., Deuss, A., and Van Heijst, H.-J. (2016). SP12RTS: a degree-12 model of shear-and compressional-wave velocity for Earth's mantle. *Geophys. J. Int.* , 204(2):1024–1039.

Laske, G., Masters, G., Ma, Z., and Pasyanos, M. (2013). Update on crust1. 0—a 1-degree global model of earth's crust. In *Geophys. res. abstr*, volume 15, page 2658.

Lekić, V. and Romanowicz, B. (2011). Inferring upper-mantle structure by full waveform tomography with the spectral element method. *Geophysical Journal International*, 185(2):799–831.

Lu, C. and Grand, S. P. (2016). The effect of subducting slabs in global shear wave tomography. *Geophys. J. Int.* , 205(2):1074–1085.

Montelli, R., Nolet, G., Dahlen, F., and Masters, G. (2006). A catalogue of deep mantle plumes: New results from finite-frequency tomography. *Geochemistry, Geophysics, Geosystems*, 7(11).

Mooney, W., Laske, G., and Masters, T. (1998). CRUST 5.1: A global crustal model at 5× 5 °. *J. Geophys. Res.* , 103(B1):727–747.

Moulik, P. and Ekström, G. (2014). An anisotropic shear velocity model of the Earth's mantle using normal modes, body waves, surface waves and long-period waveforms. *Geophys. J. Int.* , 199(3):1713–1738.

Panning, M., Lekić, V., and Romanowicz, B. (2010). Importance of crustal corrections in the development of a new global model of radial anisotropy. *J. Geophys. Res.* , 115(B12).

Ritsema, J., Deuss, A., van Heijst, H.-J., and Woodhouse, J. H. (2011). S40RTS: a degree-40 shear-velocity model for the mantle from new Rayleigh wave dispersion, teleseismic traveltime and normal-mode splitting function measurements. *Geophys. J. Int.* , 184(3):1223–1236.

Ritsema, J., van Heijst, H.-J., and Woodhouse, J. (1999). Complex shear wave velocity structure imaged beneath Africa and Iceland. *Science* , 286(5446):1925.

Simmons, N. A., Forte, A. M., Boschi, L., and Grand, S. P. (2010). GyPSuM: A joint tomographic model of mantle density and seismic wave speeds. *J. Geophys. Res.* , 115(B12).

Tesoniero, A., Auer, L., Boschi, L., and Cammarano, F. (2015). Hydration of marginal basins and compositional variations within the continental lithospheric mantle inferred from a new global model of shear and compressional velocity. *J. Geophys. Res.* , 120(11):7789–7813.